Journal Pre-proof

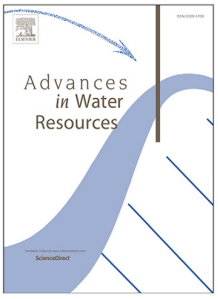

Coupled two-phase flow and surfactant/PFAS transport in porous media with angular pores: From pore-scale physics to Darcy-scale modeling

Sidian Chen, Bo Guo, Tianyuan Zheng

PII: S0309-1708(26)00018-7
DOI: https://doi.org/10.1016/j.advwatres.2026.105222
Reference: ADWR 105222

To appear in: *Advances in Water Resources*

Received date : 11 September 2025
Revised date : 13 January 2026
Accepted date : 25 January 2026

Please cite this article as: S. Chen, B. Guo and T. Zheng, Coupled two-phase flow and surfactant/PFAS transport in porous media with angular pores: From pore-scale physics to Darcy-scale modeling. *Advances in Water Resources* (2026), doi: https://doi.org/10.1016/j.advwatres.2026.105222.

Highlights

Coupled two-phase flow and surfactant/PFAS transport in porous media with angular pores: From pore-scale physics to Darcy-scale modeling

Sidian Chen, Bo Guo, Tianyuan Zheng

- Derive two-phase flow properties for surfactant/PFAS-laden fluids in angular porous media using a bundle-of-capillary-tubes model
- Formulate the two-phase flow properties as functions of interfacial tension, contact angle, and pore geometry and size distribution
- Derive explicit expressions and closed-form functions for the two-phase flow properties
- Couple explicit expressions and closed-form functions into a Darcy-scale two-phase flow and surfactant/PFAS transport model
- Example simulations highlight the critical role of pore angularity in PFAS transport and retention in unsaturated soils

Coupled two-phase flow and surfactant/PFAS transport in porous media with angular pores: From pore-scale physics to Darcy-scale modeling

Sidian Chen[a,*], Bo Guo[b], Tianyuan Zheng[c,d]

[a] *Department of Energy Science & Engineering, Stanford University, 367 Panama St, Stanford, CA, 94305, United States*
[b] *Department of Hydrology & Atmospheric Sciences, University of Arizona, Tucson, AZ, 85721, USA*
[c] *College of Environmental Science and Engineering, Ocean University of China, Qingdao, 266100, China*
[d] *Key Laboratory of Marine Environment and Ecology, Ministry of Education, Ocean University of China, Qingdao, 266100, China*

Abstract

Two-phase surfactant-laden flow and transport in porous media are central to many natural and engineering applications. Surfactants modify two-phase flow by altering interfacial tension and wettability, while two-phase flow controls surfactant transport pathways and adsorption sites. These coupled processes are commonly modeled by combining Darcy-type two-phase flow equations with advection–dispersion–adsorption transport equations, with capillary pressure–saturation relationships scaled using the Leverett J-function. However, the Leverett J-function simplifies the porous medium as bundles of cylindrical tubes and decouples interfacial tension and wettability, limiting representation of angular pore geometries and coupled interfacial tension and wettability effects. We present a modeling framework that incorporates pore angularity and interfacial tension–wettability coupling ef-

*Corresponding author.
Email address: sidianc@stanford.edu (Sidian Chen)

fect into Darcy-scale surfactant-laden flow and transport models. Within this framework, we derive two-phase flow properties for angular pores, upscale them across pore size distributions, and obtain explicit and closed-form expressions for the upscaled properties. These expressions are incorporated into a coupled flow–transport model for simulating transient two-phase flow and surfactant transport processes. Results suggest a nonmonotonic and nonlinear dependence of two-phase flow properties on pore structure (angularity and size distribution) and interfacial tension (controlled by surfactant type and concentration). Example simulations of water flow and PFAS (surfactant-like contaminants) migration in unsaturated soils indicate that surfactant-induced flow effects on PFAS leaching are generally minor under typical site conditions, whereas pore angularity exerts dominant control on water flow, interfacial area, and consequently PFAS retention. Overall, the upscaling framework offers a more physically grounded approach for modeling two-phase surfactant-laden fluid flow and surfactant transport in porous media.

Keywords: Surfactant, Per- and polyfluoroalkyl substances (PFAS), Interfacial tension, Contact angle, Angular pores, Upscaling

1. Introduction

Two-phase surfactant-laden fluid flow and surfactant transport in porous media play an important role in many natural and industrial applications. Surfactants can reduce interfacial tension between fluids and alter solid surface wettability through interfacial adsorption, which may alter fluid flow through porous structures. Fluid flow, in turn, controls the advection and diffusion of surfactants and governs the fluid-fluid and fluid–solid interfaces that facilitate the interfacial adsorption of surfactants. These mechanisms

have been harnessed to remove pollutants (e.g., non-aqueous phase liquid (NAPL) and per- and polyfluoroalkyl substances (PFAS)) from soils and groundwater (e.g., Al-Raoush, 2009; Maroli et al., 2024), enhance oil and gas recovery (e.g., Pope and Nelson, 1978; Lake, 1989), improve CO_2 and hydrogen storage efficiency (e.g., Føyen et al., 2020; Chaturvedi et al., 2022), and optimize fluid behavior in manufactured porous materials such as cooling systems and CO_2 capture electrolyzers (e.g., Ge et al., 2022). Consequently, mechanistic understandings and accurate predictions of the coupled two-phase flow and surfactant transport are essential for advancing technologies in these environmental, energy, and climate applications.

Modeling surfactant-laden fluid flow in porous media is challenging due to the nonlinear coupling between fluid flow and surfactant transport. A common strategy is to couple Darcy-scale two-phase flow with surfactant transport (e.g., Pope and Nelson, 1978; Abriola et al., 1993; Smith and Gillham, 1994), where flow is described by two-phase extended Darcy's law (or simplified forms such as Richards' equation) and transport is governed by advection–dispersion–adsorption equations. Most models did not account for surfactant adsorption at fluid-fluid interfaces. Surfactant effects are typically incorporated by scaling the capillary pressure–saturation relationship with the Leverett J-function (i.e., $J(S) \propto 1/(\gamma \cos\theta)$, where S is fluid saturation, θ the contact angle, and γ the fluid–fluid interfacial tension), while other flow properties such as relative permeability and interfacial area–saturation relations are usually assumed unchanged (e.g., Smith and Gillham, 1994).

The Leverett J-function, originally derived semi-empirically by Leverett (1941), relies on two major simplifications. First, it represents pore spaces as bundles of cylindrical tubes, whereas many porous media exhibit angular geometries that may strongly alter fluid configurations, capillary pressure,

relative permeability, and interfacial area. Second, it assumes that interfacial tension and contact angle are independent, which may break down when surfactants are present. Surfactant adsorption modifies fluid–fluid and solid–fluid interfacial tensions, thereby altering the contact angle. Accounting for pore angularity and the coupling between interfacial tension and contact angle is critical for more accurate predictions of two-phase flow properties of different surfactant-free fluid systems (e.g., Tokunaga et al., 2013; Wang et al., 2016).

The impact of pore angularity on two-phase surfactant-free fluid flow is well established through experiments (e.g., Dong and Chatzis, 1995; Øren and Bakke, 2003) and pore-scale and upscaling simulations (e.g., Tuller et al., 1999; Diamantopoulos and Durner, 2013, 2015; Jiang et al., 2020a,b). In contrast, two-phase flow of surfactant-laden fluids in angular porous media remains underexplored (Wijnhorst et al., 2020). Existing studies rely mainly on experiments and empirical models (e.g., Desai et al., 1991; Karagunduz et al., 2001), which are difficult to generalize across pore structures, wettability conditions, surfactant chemistries, and concentrations. This highlights the need to develop predictive pore-scale and upscaling models for deriving two-phase flow properties under diverse conditions and improving coupled two-phase flow–surfactant transport frameworks.

Among the modeling approaches, the bundle-of-capillary-tubes model provides an attractive framework. It can efficiently quantify flow and transport properties at the representative elementary volume (REV) scale (e.g., Diamantopoulos and Durner, 2013), yielding explicit and/or closed-form expressions that can be directly integrated into Darcy-scale models (Diamantopoulos and Durner, 2015). Moreover, it captures the effects of pore angularity for surfactant-free fluids with good agreements with experimental

observations (e.g., Or and Tuller, 1999; Tuller and Or, 2001; Diamantopoulos and Durner, 2013; Jiang et al., 2020b). Building on this foundation, we extend the bundle-of-capillary-tubes concept to develop an upscaling workflow for deriving REV-scale two-phase flow properties of surfactant-laden fluids in angular porous media and integrating the derived properties into Darcy-scale coupled flow and transport models. This upscaling workflow consists of four key steps: (1) compute surfactant-laden fluid configurations in a single angular pore represented by a angular tube; (2) derive the upscaled two-phase flow properties for a porous medium whose void spaces are represented by a bundle of tubes; (3) formulate explicit expressions and closed-form functions for the new properties; and (4) integrate these expressions into Darcy-scale flow and surfactant transport models. This is the first framework that explicitly integrates pore angularity and interfacial tension–contact angle coupling into Darcy-scale two-phase flow surfactant transport models.

We demonstrate the workflow's potential by applying it to a representative case: PFAS transport in unsaturated soils. PFAS, a class of fluorinated surfactant contaminants, have raised global health concerns due to their ubiquity, persistence, bioaccumulation, and toxicity at ng/L concentrations. Predicting their migration in soils remains challenging because it is governed by the coupled effects of interfacial interactions, surface tension variations, and transient unsaturated flow within irregular, often angular, pore spaces (Figure 1). Existing numerical models—typically based on Richards' equation coupled with advection–dispersion–adsorption formulations—account for surface tension effects only through scaling the capillary pressure–saturation curve using the standard Leverett J-function (e.g., Guo et al., 2020; Silva et al., 2020; Zeng and Guo, 2021). These approaches inherently neglect the influence of pore angularity and the coupling between interfacial tension and

contact angle, both of which may strongly affect two-phase flow properties and PFAS transport. We employ our framework to quantify how these factors regulate PFAS migration in unsaturated soil columns under laboratory conditions, providing insights for future field-scale modeling efforts.

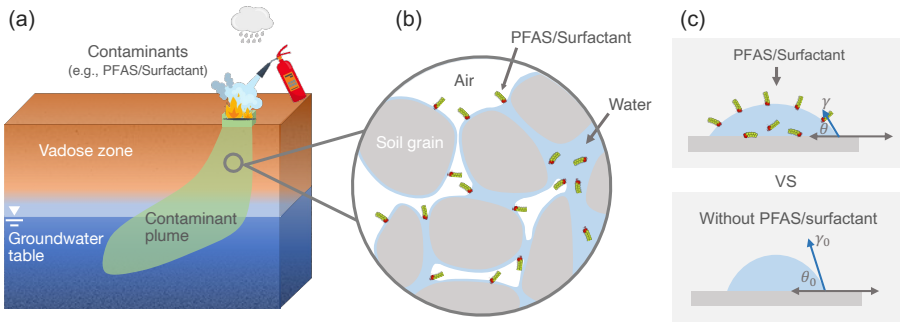

Figure 1: (a) Schematic of soil contamination by surfactant-like chemicals, such as per- and polyfluoroalkyl substances (PFAS). (b) Accumulation and adsorption of PFAS at the air–water interfaces in unsaturated soil pores. (c) Surface tension and contact angle of PFAS-laden water compared with PFAS-free water. Panels (a) and (b) are revised from Chen and Guo (2023) with permission of the authors and Wiley.

2. Methods

2.1. Interfacial tension and contact angle for surfactant-laden fluids

For two fluids (i.e., a wetting-phase fluid and a nonwetting-phase fluid) that are surfactant-free and resting on a solid surface, the interfacial forces at the three-phase contact line follow Young–Dupré equation (Young, 1805; Dupré and Dupré, 1869)

$$\gamma_{wn,0} \cos\theta_0 = \gamma_{sn,0} - \gamma_{sw,0}, \tag{1}$$

where $\gamma_{wn,0}$, $\gamma_{sn,0}$, and $\gamma_{sw,0}$ are the interfacial tension between surfactant-free fluids, the interfacial tension between solid and surfactant-free nonwetting-phase fluid, and the interfacial tension between solid and surfactant-free wetting-phase fluid, respectively; θ_0 is the intrinsic contact angle between the solid and surfactant-free fluids.

When surfactants are present, they can adsorb at the fluid–fluid and fluid–solid interfaces, altering their interfacial tensions. Because the interfacial forces at the three-phase contact line remain balanced, we obtain

$$\gamma_{wn}\cos\theta = \gamma_{sn} - \gamma_{sw}, \tag{2}$$

where γ_{wn}, γ_{sn}, and γ_{sw} are the interfacial tension between surfactant-laden solid and surfactant-laden nonwetting-phase fluid, the interfacial tension between surfactant-laden solid and surfactant-laden wetting-phase fluid, and the interfacial tension between surfactant-laden fluids, respectively; and θ is the contact angle in the presence of interfacial adsorption of surfactants. Note that if $\gamma_{wn} > |\gamma_{sn} - \gamma_{sw}|$, the surface is partially wet to the wetting-phase fluid. Once γ_{wn} becomes smaller than $|\gamma_{sn} - \gamma_{sw}|$, the contact line disappears and the solid surface is completely wet by the wetting-phase fluid.

In Equation (2), γ_{wn} can be given by the Szyszkowski equation,

$$\gamma_{wn} = \gamma_{wn,0}\left[1 - b_\alpha \ln\left(1 + \frac{C_\alpha}{a_\alpha}\right)\right], \tag{3}$$

where C_α is the surfactant concentration in the wetting-phase fluid ($\alpha = w$) or nonwetting-phase fluid ($\alpha = nw$), and a_α and b_α are model parameters obtained via fitting to measured surface tension data. Accordingly, we can compute the fluid–fluid interfacial excess (Γ_{wn}) via the Gibbs equation (i.e., $\Gamma_{wn} = -\frac{1}{R_g T}\frac{\partial \gamma_{wn}}{\partial \ln C_\alpha}$, where R_g is the universal gas constant, T is temperature), which yields $\Gamma_{wn} = \gamma_{wn,0} b_\alpha C_\alpha / [R_g T(a_\alpha + C_\alpha)]$. Additionally, assuming the solid–fluid interfacial adsorption follows the Freundlich isotherm

(i.e., $\Gamma_{s\alpha} = K_{f,\alpha} C_\alpha^{N_{f,\alpha}}$, where $\gamma_{s\alpha}$ is the surfactant excess at the fluid–solid interfaces, $K_{f,\alpha}$ and $N_{f,\alpha}$ are fitting parameters with experimental measurements), we can derive a Freundlich analog of the Szyszkowski equation for γ_{SN} and γ_{SW} by plugging the Freundlich isotherm and Gibbs equation and integrating with respect to the surfactant concentration,

$$\gamma_{s\alpha} = \gamma_{s\alpha,0} - \int_0^{C_\alpha} R_g\, T\, \Gamma_{s\alpha}(C)\, \mathrm{d} \ln C = \gamma_{s\alpha,0} - \frac{R_g T K_{f,\alpha}}{N_{f,\alpha}} C_\alpha^{N_{f,\alpha}}, \qquad (4)$$

where $\Gamma_{s\alpha}$ is the surfactant excess at the interface between solid and wetting-phase fluid ($\alpha = w$) or at the interface between solid and nonwetting-phase fluid ($\alpha = nw$). It is worth noting that Equations (3) and (4) predict monotonic decreases in γ_{wn} and $\gamma_{s\alpha}$ as surfactant concentration increases. In practice, these interfacial tensions often level off above a characteristic concentration (e.g., the critical micelle concentration). Capturing this behavior requires modified expressions (e.g., asymptotic forms), which are not considered in the present study.

Because γ_{wn} and θ—which collectively control the capillary pressure and fluid configuration in the pore spaces—are functions of surfactant concentrations, the two-phase flow properties (i.e., the relationships among capillary pressure, relative permeability, and fluid–fluid interfacial area, and fluid saturation) will depend on the surfactant concentrations. We derive the two-phase flow properties for surfactant-laden fluids using a bundle-of-capillary-tubes model (Figure 2a–c). In particular, the model represents the complex pore structures in a porous medium by a bundle of capillary tubes with idealized geometries. Following this simplified representation, we can derive two-phase flow properties for surfactant-laden fluids in an individual pore of a porous medium and upscale the individual-pore relationships for the porous medium with an arbitrary pore size distribution. The specific

procedures are explained in the following sections

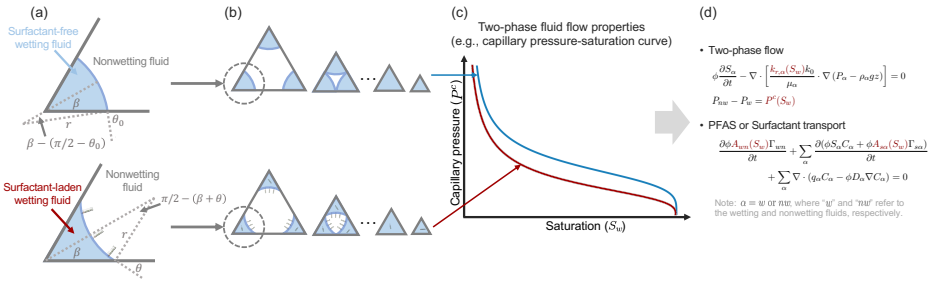

Figure 2: A upscaling workflow to bridge pore-scale physics of coupled two-phase flow and surfactant/PFAS transport into a Darcy-scale modeling framework. The workflow consists of four steps: (a) Compute the configuration of the wetting and nonwetting fluids in an angular corner for a given capillary pressure with or without the presence of surfactant/PFAS in the fluids. Equilateral triangular tubes are used as examples. (b) Compute the configuration of the wetting and nonwetting fluids in a bundle of capillary tubes for a given capillary pressure. (c) Apply the bundle-of-capillary-tubes model to derive two-phase flow properties (e.g., capillary pressure, relative permeability, and fluid–fluid interfacial area vs. fluid saturation curves) for a porous medium. The capillary pressure vs. wetting-phase fluid saturation curve is used as an example. (d) Couple the new two-phase flow properties into Darcy-scale transient two-phase flow and surfactant/PFAS transport models. Note that a nanometer-scale thin wetting-phase fluid film (referred to as "precursor film") may form on partially-wet surfaces, while a macroscopic thin wetting-phase fluid film (thicker than precursor film) will form on completely-wet surfaces. Due to the small film thickness, the thin films are not shown in Panels (a) and (b).

2.2. Two-phase flow properties in a pore with varying geometries

We first derive the two-phase flow properties for surfactant-laden fluids in an individual pore with idealized geometries (e.g., cylindrical, square, and triangular tubes).

2.2.1. Capillary pressure

We start from a pore that is saturated by the wetting-phase fluid and is connected to a reservoir of a nonwetting-phase fluid. As we increase the reservoir pressure, the nonwetting-phase fluid will invade the pore when the pressure difference between nonwetting- and wetting-phase fluids (i.e., the capillary pressure p^c) exceeds a threshold (referred to as "critical capillary pressure p^c_{cr}" hereafter). In a cylindrical pore, p^c_{cr} is given by (Dullien, 2012)

$$p^c_{cr} = \frac{\gamma_{wn}\cos\theta}{2R}, \tag{5}$$

where R is the radius of the circular cross-section of the cylindrical pore. In an angular pore, p^c_{cr} is assumed equal to the p^c where the fluid-fluid interfaces meet in the angular pore, which is given by

$$p^c_{cr} = \frac{\gamma_{wn}}{r_c} \tag{6}$$

where r_c is the radius of curvature when the menisci meet and collapse at the edges of the cross-sections of a pore. The expression of r_c depends on the pore geometries. In a square-tube pore, r_c is given by (Chen et al., 2020)

$$r_c = \frac{R\sin(\pi/4)}{|\sin(\pi/4-\theta)|}, \tag{7}$$

where R is the inscribed radius of the cross-section of the square-tube pore. The r_c in a triangular-tube pore is given by

$$r_c = \min_{\substack{i,j\in\{1,2,3\}\\ \&\ i\neq j}} \left(\frac{R(\cot\beta_i + \cot\beta_j)}{|\sin(\pi/2-\beta_i-\theta)|/\sin\beta_i + |\sin(\pi/2-\beta_j-\theta)|/\sin\beta_j} \right), \tag{8}$$

where β_i and β_j refer to i^{th} and j^{th} half corner angles, respectively; R is the inscribed radius of the cross-section of the triangular-tube pore.

When $p^c \leq p^c_{cr}$ in a pore, the pore is saturated by the wetting-phase fluid. Once p^c exceeds p^c_{cr}, the nonwetting-phase fluid invades the pore. The

wetting-phase fluid will either reside at the corners of angular pores (referred to as "corner" fluid hereafter) or form thin fluid films on the solid surfaces not covered by bulk or corner fluids. Two types of thin fluid films may form. In a partially-wet pore, the wetting-phase fluid may form a nanometer-scale thin film on the surface (referred to as "precursor" film hereafter) due to surface adsorption, capillary condensation, surface roughness, or surface heterogeneity. In a completely wet pore, the wetting-phase fluid will spread on the surface and form a macroscopic thin film (referred to as "macroscopic" film hereafter) that is thicker than the precursor film. Because the films are often extremely thin, their volumes are almost negligible (if they exist) compared with the total fluid volume, we neglect their contribution to the overall saturation. Accordingly, the wetting-phase fluid saturation in an invaded cylindrical pore is assumed to be zero, while that in an invaded angular pore is given by

$$s_w = \frac{r^2 \tilde{A}_c}{R^2 \sum_{i=1}^{N_\beta} \cot \beta_i}, \tag{9}$$

where r is the radius of meniscus curvature given by $r = \gamma_{wn}/p^c$, N_β is the number of corners of the cross-section of the angular pore (e.g., $N_\beta = 3$ in a triangular-tube pore and $N_\beta = 4$ in a square-tube pore), β_i is the half-corner angle, and $\tilde{A}_c$ is the dimensionless cross-sectional area of a pore with $r = 1$ and $\tilde{A}_c$ is given by

$$\tilde{A}_c = \sum_{i=1}^{N_\beta} \left[\frac{\sin(\pi/2 - \beta_i - \theta)}{\sin \beta_i} \cos\theta - (\pi/2 - \beta_i - \theta) \right]. \tag{10}$$

The nonwetting-phase fluid saturation is given by

$$s_{nw} = 1 - s_w. \tag{11}$$

2.2.2. Relative permeability

If a pore is saturated by a fluid, the permeability is given by (Patzek, 2001; Patzek and Kristensen, 2001)

$$k_\alpha = \eta G A_\alpha^2, \tag{12}$$

where η is the corrector varying with pore geometry ($\eta = 0.5, 0.5623$, or 0.6 for cylindrical, square-tube, and equal-lateral triangular-tube pores, respectively), G is the shape factor of the pore cross-section (i.e., the area divided by perimeter square), A_α is the area of fluid α in the cross-section of a pore, and α indicates the fluid of interest (i.e., $\alpha = w$ indicates the wetting-phase fluid, while $\alpha = nw$ indicates the nonwetting-phase fluid).

If two fluids coexist in a pore, the wetting-phase fluid will reside either as thin films in cylindrical pores or as corner fluid and thin films in angular pores. We assume the thin film permeability is negligible. In a cylindrical pore invaded by the nonwetting-phase fluid, the wetting-phase fluid permeability is 0, while the nonwetting-phase fluid permeability is given by Equation (12). In an angular pore invaded by nonwetting-phase fluid, the corner fluid contributes a non-negligible permeability, which is given by (Patzek, 2001)

$$k_w = 2\sum_{i=1}^{N_\beta} k_{w,i} = 2\sum_{i=1}^{N_\beta} \tilde{g}_{w,i} l_{w,i}^4, \tag{13}$$

where $k_{w,i}$ is the wetting-phase fluid permeability in a half corner with an angle of β_i, $l_{w,i}$ is the wetting-phase meniscus-apex distance along the wall at the i^{th} corner (i.e., $l_{w,i} = r|\sin(\pi/2 - \beta_i - \theta)|/\sin\beta_i$), and $\tilde{g}_w$ is the dimensionless conductance of the wetting phase at the half corner (β_i) with a unit meniscus-apex distance (i.e., $l_{w,i} = 1$). The nonwetting-phase fluid

residing in the middle of the pore is given by (Qin and van Brummelen, 2019)

$$k_{nw} = \eta G A_{nw}^2 s_{nw}^2. \tag{14}$$

2.2.3. Fluid–fluid interfacial area

In a cylindrical pore, fluid–fluid interfaces will arise from thin films. Assuming the surfaces are smooth, the fluid–fluid interfacial area a_{wn} in an invaded cylindrical pore with a unit length is given by

$$a_{wn} = 2\pi R, \tag{15}$$

where R is the radius of the pore that is invaded by nonwetting-phase fluid. In an angular pore, fluid–fluid interfaces will arise from both corner water and thin films. Because the thin-film fluid–fluid interfaces are comparable or even larger than those associated with the corner water, they should be accounted for in the calculation of a_{wn}. Assuming the surfaces are smooth, the fluid–fluid interfacial area a_{wn} in an angular pore with a unit length is given by

$$a_{wn} = 2\sum_{i=1}^{N_\beta} \left(r \cdot |\pi/2 - \beta_i - \theta| + R - l_{w,i} \right), \tag{16}$$

where $l_{w,i}$ is the wetting-phase meniscus-apex distance along the wall at the i^{th} corner and can be calculated via Equation (13).

2.3. Two-phase flow properties in a porous medium

We then upscale the individual-pore two-phase flow properties for a porous medium through a bundle-of-capillary-tubes model. Assuming the pores in a porous medium share the same intrinsic contact angle ($\gamma_{wn,0}$) and the pore sizes follow a distribution given by $f(R)$ with R being the inradius of the cross-section of a pore and f being the probability density of pores

whose cross-sectional inradius is equal to R, the upscaled two-phase flow properties in a porous medium can be computed via an integration over the pore size distribution.

In particular, we compute the wetting-phase fluid saturation (S) as a function of capillary pressure (P^c) for a porous medium by integrating the individual-pore saturation over the pore size distribution, which yields

$$S = \frac{\int f(R) \cdot v(R) \cdot s(R, P^c, \gamma_{wn}) \, \mathrm{d}R}{\int f(R) \cdot v(R) \, \mathrm{d}R}, \tag{17}$$

where v is the pore volume and s is computed given that $p^c = P^c$.

Similarly, we compute the relative permeability under a macroscopic capillary pressure P^c (and correspondingly saturation S) by taking the ratio between the cumulative permeability for a fluid in each pore and the permeability for the entire porous medium under saturated conditions, which is given by

$$k_{r,\alpha} = \frac{\int f(R) \cdot k_\alpha(R, P^c, \gamma_{wn}) \, \mathrm{d}R}{\int f(R) \cdot k_0(R) \, \mathrm{d}R}, \tag{18}$$

where s is the saturation of the fluid of interest, which is a function of R, P^c, and γ_{wn} for a given $\gamma_{wn,0}$ and θ_0. Finally, we can combine Equations (17) and (18) to compute the k_r-S curves.

Similarly, we compute the fluid–fluid interfacial area per unit pore volume under a macroscopic capillary pressure P^c (and correspondingly saturation S) by integrating those in all pores, which yields

$$A_{wn} = \frac{\int f(R) \cdot a_{wn}(R, P^c, \gamma_{wn}) \, \mathrm{d}R}{\int f(R) \cdot A_0(R) \, \mathrm{d}R}, \tag{19}$$

We can also combine Equations (17) and (19) to compute the A_{wn}-S curves.

While Equations (17–19) provide the upscaled two-phase flow properties in porous media with arbitrary pore size distributions, simplified mathematical representations are desired to couple them into two-phase flow and

transport models. The following section introduces their simplified mathematical representations under idealized conditions.

2.4. Simplified mathematical representations of two-phase flow properties

We consider a porous medium with uniform intrinsic contact angles, uniform pore geometries (i.e., cylinders, square tubes, or triangular tubes with angle-angle similarity), and log-normal pore size distributions. Accordingly, we can derive explicit expressions and closed-form functions for the two-phase flow properties.

2.4.1. Explicit expressions

We drive the explicit functions for capillary pressure, relative permeability, and fluid-fluid interfacial area in the porous medium.

Capillary pressure-saturation curve. We first derive the scaling function for the capillary pressure in a porous medium with a log-normal pore size distribution. Suppose $R_{\max}$ is the maximum size of the saturated pores that are not invaded. Then the saturation is given by

$$S = \frac{\tilde{A}_0 \int_0^{R_{\max}} f(R) R^2 \, \mathrm{d}R + \tilde{A}_c r^2 \int_{R_{\max}}^{\infty} f(R) \, \mathrm{d}R}{\tilde{A}_0 \int_0^{\infty} f(R) R^2 \, \mathrm{d}R} \tag{20}$$

where $\tilde{A}_0$ is the dimensionless cross-sectional area of a pore with $R = 1$ (i.e., $\tilde{A}_0 = \pi$ for a cylindrical pore, $\tilde{A}_0 = 4$ for a square-tube pore, $\tilde{A}_0 = \sum_{i=1}^{3} \cot \beta_i$ for a triangular-tube pore), A_c is the area of the fluid in the corner of an unsaturated angular pore and $A_c = 0$ if the pore is represented by a cylindrical tube, and $f(R)$ is the probability density function (PDF) of the pore sizes. $f(R)$ is given by

$$f(R) = \frac{1}{R\sigma\sqrt{2\pi}} \exp\left(-\frac{(\ln R - \mu)^2}{2\sigma^2}\right), \tag{21}$$

where μ and σ are the mean and standard deviation of the natural log of the pore size R.

To evaluate S, we need to compute $\int_0^{R_{\max}} f(R)R^2\,\mathrm{d}R$ and $\int_{R_{\max}}^{\infty} f(R)\,\mathrm{d}R$ from the following equation,

$$\begin{aligned}\int_0^{R_{\max}} f(R)R^n\,dR &= e^{n\mu+\frac{1}{2}n^2\sigma^2}\cdot\Phi\left(\frac{\ln R_{\max}-(\mu+n\sigma^2)}{\sigma}\right),\\ \int_{R_{\max}}^{\infty} f(R)R^n\,\mathrm{d}R &= e^{n\mu+\frac{1}{2}n^2\sigma^2}\cdot\left[1-\Phi\left(\frac{\ln R_{\max}-(\mu+n\sigma^2)}{\sigma}\right)\right],\end{aligned} \tag{22}$$

where n denotes the exponent (power) of R within the integrand, and Φ is the cumulative distribution function of the standard normal distribution.

Relative permeability-saturation curve. The wetting-phase relative permeability is given by

$$k_{r,w}=\frac{\eta G\tilde{A}_0^2\int_0^{R_{\max}} f(R)R^4\,\mathrm{d}R+\left(2\sum_{i=1}^{N_\beta}\tilde{g}_{1,i}l_{1,i}^4\right)\int_{R_{\max}}^{\infty} f(R)\,\mathrm{d}R}{\eta G\tilde{A}_0^2\int_0^{\infty} f(R)R^4\,\mathrm{d}R}, \tag{23}$$

while that of the non-wetting phase is given by

$$k_{r,nw}=\frac{\tilde{A}_0^2\int_{R_{\max}}^{\infty} f(R)R^4\,\mathrm{d}R-2\tilde{A}_0\tilde{A}_c r^2\int_{R_{\max}}^{\infty} f(R)R^2\,\mathrm{d}R+\tilde{A}_c^2 r^4\int_{R_{\max}}^{\infty} f(R)\,\mathrm{d}R}{\tilde{A}_0^2\int_0^{\infty} f(R)R^4\,\mathrm{d}R}, \tag{24}$$

where $\int_0^{R_{\max}} f(R)R^4\mathrm{d}R$, $\int_{R_{\max}}^{\infty} f(R)\mathrm{d}R$, $\int_{R_{\max}}^{\infty} f(R)R^2\mathrm{d}R$, and $\int_{R_{\max}}^{\infty} f(R)R^4\mathrm{d}R$ are given by Equation (22)

Fluid-fluid interfacial area-saturation curve. Finally, we can compute the specific fluid-fluid interfacial area (i.e., the fluid-fluid interfacial area normalized by the total pore volume) for cylindrical tubes by

$$A_{wn}=\frac{2\pi\int_{R_{\max}}^{\infty} f(R)R\,\mathrm{d}R}{\tilde{A}_0\int_0^{\infty} f(R)R^2\,\mathrm{d}R}, \tag{25}$$

and that for angular tubes by

$$A_{wn}=\frac{\left(a_{wn}^c-2\sum_{i=1}^{N_\beta} l_{w,i}\right)\int_{R_{\max}}^{\infty} f(R)\,\mathrm{d}R+2N_\beta\int_{R_{\max}}^{\infty} f(R)R\,\mathrm{d}R}{\tilde{A}_0\int_0^{\infty} f(R)R^2\,\mathrm{d}R}, \tag{26}$$

where $\int_{R_{\max}}^{\infty} f(R)\,\mathrm{d}R$ and $\int_{R_{\max}}^{\infty} f(R)R\,\mathrm{d}R$ are given by Equation (22).

Equations (20) and (23–26) provide the explicit expressions for the two-phase flow properties in porous media with a uniform wettability, uniform pore geometry, and lognormal pore size distribution.

2.4.2. Closed-form functions

The explicit expressions are given as functions of the cumulative normal distribution functions. We can approximate the cumulative normal distribution functions by closed-form functions such as a logistic function $\Phi(x) \approx 1/[1 + \exp(-1.702x)]$. This approximation allows for obtaining closed-form functions for the upscaled two-phase flow properties and conveniently coupling them into transient two-phase flow models.

2.5. Coupled Darcy-scale two-phase flow and surfactant/PFAS transport model

We introduce the transient two-phase flow and surfactant transport models that couple the new two-phase flow properties, as well as the numerical algorithm for solving the model.

2.5.1. Two-phase flow model

We describe the two-phase flow by an extended two-phase Darcy model,

$$\phi \frac{\partial S_\alpha}{\partial t} + \nabla \cdot q_\alpha = 0 \tag{27}$$

where $q_\alpha = -k_{r,\alpha} k_0 \mu_\alpha^{-1} \cdot \nabla \left(P_\alpha - \rho_\alpha g z\right)$, $k_{r,\alpha}$ are computed via Equations (23–24), k_0 is the absolute permeability, P_α is the pressure of α phase, P_α is constrained by $P_n - P_w = P^c$ with P^c being given by Equation (20), z is the spatial coordinate (assuming positive downward).

2.5.2. Surfactant and PFAS transport model

The surfactants can dissolve in the fluids, migrate with the fluid flow via advection and dispersion, and adsorb onto or desorb from the fluid–fluid and fluid–solid interfaces. We consider a single-component surfactant system and instantaneous interfacial adsorption. Subsequently, the governing equation for surfactant transport is given by

$$\frac{\partial \phi A_{wn} \Gamma_{wn}}{\partial t} + \sum_{\alpha} \left[\frac{\partial (\phi S_\alpha C_\alpha + \phi A_{s\alpha} \Gamma_{s\alpha})}{\partial t} + \nabla \cdot (q_\alpha C_\alpha - \phi S_\alpha D_\alpha \nabla C_\alpha) \right] = 0, \tag{28}$$

where D_α is the dispersion coefficient in the α (i.e., $D_\alpha = \tau D_{0,\alpha} + \mathcal{L}_\alpha |q_\alpha/\phi/S_\alpha|$, where τ is the tortuosity which can be approximated as $\tau = (\phi S_\alpha)^{7/3}/\phi^2$ (Millington and Quirk, 1961), $D_{0,\alpha}$ is the molecular diffusion coefficient in free α phase, $\mathcal{L}_\alpha$ is the longitudinal dispersivity, Γ_{wn} and $\Gamma_{s\alpha}$ are the surfactant excess at fluid–fluid and solid–fluid interfaces, respectively. Γ_{wn} and $\Gamma_{s\alpha}$ are given by the Langmuir and Freundlich isotherms as discussed in Section 2.1.

2.5.3. Numerical algorithm

Equations (27) and (28) represent the two-phase flow and surfactant transport models. The model has three primary unknown variables: P_α, P^c (or S_α), and C_α, where $\alpha = w$ or nw. They can be solved with well-imposed initial and boundary conditions. We solve the unknown variables using a backward-Euler finite difference method. At each time step, the resulting nonlinear discretized equations are solved iteratively using the Newton-Raphson method. The convergence of the iterations is accepted when the L_∞-norm of the residuals and the L_∞-norm of the updates of the primary variables (e.g., P_α, P^c, and C_α) are smaller than certain thresholds.

3. Results and analysis

We apply the bundle-of-capillary-tubes model in Section 2 to analyze the impact of fluid-fluid interfacial tension and pore geometry on two-phase flow properties in porous media (Section 3.1). Then we use the model as a reference to evaluate the accuracy of the explicit expressions and closed-form functions of the upscaled two-phase flow properties (Section 3.2). Finally, we demonstrate an example application of a two-phase fluid flow and surfactant transport model that incorporates the newly-derived two-phase flow properties (Section 3.3).

3.1. Impact of interfacial tension and pore geometry on two-phase flow properties

3.1.1. Numerical experiment design

We model the impact of interfacial tension and pore geometry on two-phase flow properties using a porous medium whose pore sizes follow a log-normal distribution, with a mean pore size of $\mu = 100\,\mu$m and a normalized standard deviation of $\sigma = 0.3$ (Figure B.1a). For illustration, we consider a near neutral-wet surface, characterized by an intrinsic contact angle of $\theta_0 = 80°$. We assume that the solid-phase adsorption of surfactants and the alteration of solid surface chemistry are weak and negligible (i.e., $\gamma_{sn} = \gamma_{sn,0}$ and $\gamma_{sw} = \gamma_{sw,0}$, and consequently $\gamma_{wn}\theta = \gamma_{wn,0}\theta_0$). This assumption is adopted to focus on the effects of fluid–fluid interfacial tension and pore geometry, rather than reflecting a model limitation, since the current model accounts for solid-phase adsorption and its impact on wettability (Section 2.1). We simulate six γ_{wn} values for cylindrical pores and nine γ_{wn} values for angular pores, ensuring that the selected values correspond to the entire range of contact angles, i.e., $0 \leq \theta \leq \theta_0$ (Figures 3–5). Note that γ_{wn} is also

a proxy of the surfactant effect, i.e., a smaller γ_{wn} corresponds to a more interfacially active surfactant and/or a higher surfactant concentration.

3.1.2. Porous media with cylindrical pores

We first analyze the impact of γ_{wn} on the two-phase flow properties in the porous medium with cylindrical pores. The results suggest a piecewise linear scaling of the capillary pressure–saturation (P^c–S_w) curves with γ_{wn} (Figure 3a–b), which falls in the following two distinct regimes:

- Regime I: $\gamma_{wn} > \gamma_{wn,0}\cos\theta_0$ (i.e., $\theta > 0$), corresponding to less interfacially active surfactants and/or lower surfactant concentrations. Because $\gamma_{wn}\cos\theta$ is constant in this regime and P^c scales linearly with $\gamma_{wn}\cos\theta$ (Equation 5), the P^c–S_w curves remain the same even γ_{wn} varies (Figure 3a).

- Regime II: $\gamma_{wn} \leq \gamma_{wn,0}\cos\theta_0$ (i.e., $\theta \equiv 0$), corresponding to more interfacially active surfactants and/or higher surfactant concentrations. Because $\cos\theta \equiv 1$ in this regime, the P^c–S_w curves become linearly scaled with γ_{wn} (Figure 3b).

In contrast, the relative permeability–saturation (k_r–S_w) and fluid–fluid interfacial area–saturation (A_{wn}–S_w) curves are the same for all γ_{wn} (Figure 3c–d). In a bundle of cylindrical tubes, each tube will be occupied by one bulk fluid and a thin precursor film of the other fluid due to the absence of corner fluids. To reach a certain S_w, the partitioning of fluids across tubes is unique. Therefore, k_r and A_{wn} are kept the same at the same S_w regardless of the varying γ_{wn}.

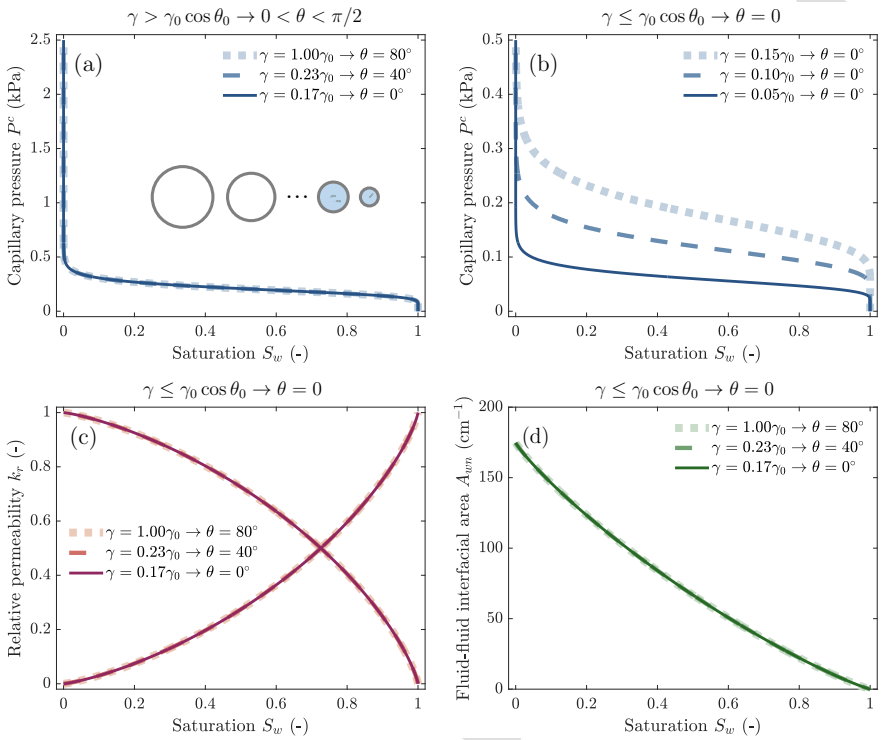

Figure 3: Impact of interfacial tension (γ_{wn}) on the (a–b) capillary pressure–saturation curves, (c) relative permeability–saturation curves, (d) fluid–fluid interfacial area–saturation curves in a porous medium with cylindrical pores. A near neutral-wet condition (e.g., an intrinsic contact angle θ_0 of 80°) is used as an illustrative example. Two γ_{wn} ranges are modeled: (1) A range within which the contact angles (θ) are greater than or near 0, and (2) A range within which $\theta \equiv 0$. Because the relative permeability–saturation curves are the same in all cases, we only show those for contact angles greater than 0. In the figure, $\gamma_{wn,0}$ refers to the interfacial tension for surfactant-free fluids. Note that γ_{wn} is a proxy of the surfactant effect, i.e., a smaller γ_{wn} corresponds to a more interfacially active surfactant and/or a higher surfactant concentration.

3.1.3. Porous media with angular pores

In porous media containing square and equilateral triangular tubes, the impact of γ_{wn} on two-phase flow properties becomes nonmonotonic and non-

linear. In particular, the impact of γ_{wn} on the P^c–S_w curves can be characterized by the following three distinct regimes:

- Regime I: $\gamma_{wn} > \gamma_{wn,0}\cos\theta_0/\cos(\pi/2-\beta)$, corresponding to less interfacially active surfactants and/or lower surfactant concentrations. In this regime, the fluid menisci are convex and the radius of meniscus curvature (r) increases with the decrease of γ_{wn}. Since P^c scales with γ/r, the decreasing γ_{wn} and increasing r lead to a decrease of P^c. Consequently, the P^c–S_w curve shifts *downwards* with the decrease of γ_{wn}, i.e., the increase of surfactant concentration (Figures 4a and 5a).

- Regime II: $\gamma_{wn,0}\cos\theta_0 < \gamma_{wn} \leq \gamma_{wn,0}\cos\theta_0/\cos(\pi/2-\beta)$, corresponding to moderately interfacially active surfactants and/or intermediate surfactant concentrations. In this regime, the menisci become concave and r begins to decrease with γ_{wn} (Figures 4b and 5b). Because $P^c \propto \gamma_{wn}/r$ and γ_{wn} decreases much less significant than r, the decrease of γ_{wn} will increase the P^c at the same S_w and thus shift the P^c–S_w curve *upwards* (Figures 4b and 5b).

- Regime III: $\gamma_{wn} \leq \gamma_{wn,0}\cos\theta_0$, corresponding to more interfacially active surfactants and/or higher surfactant concentrations. The P^c–S_w curve switches back to a *downwards* shifting mode with the further decrease of γ_{wn} given that $\theta \equiv 0$ and thus P^c–S_w curves *scale linearly* with γ_{wn} (Figures 4c and 5c).

In contrast to P^c–S_w curves, k_r–S_w and A_{wn}–S_w curves present much less significant variations with γ_{wn} (Figure 4d–i). This is because k_r and A_{wn} are mainly controlled by the fluid menisci sizes (i.e., the fluid perimeter and/or area in the cross-section of each unsaturated pore), which are much less

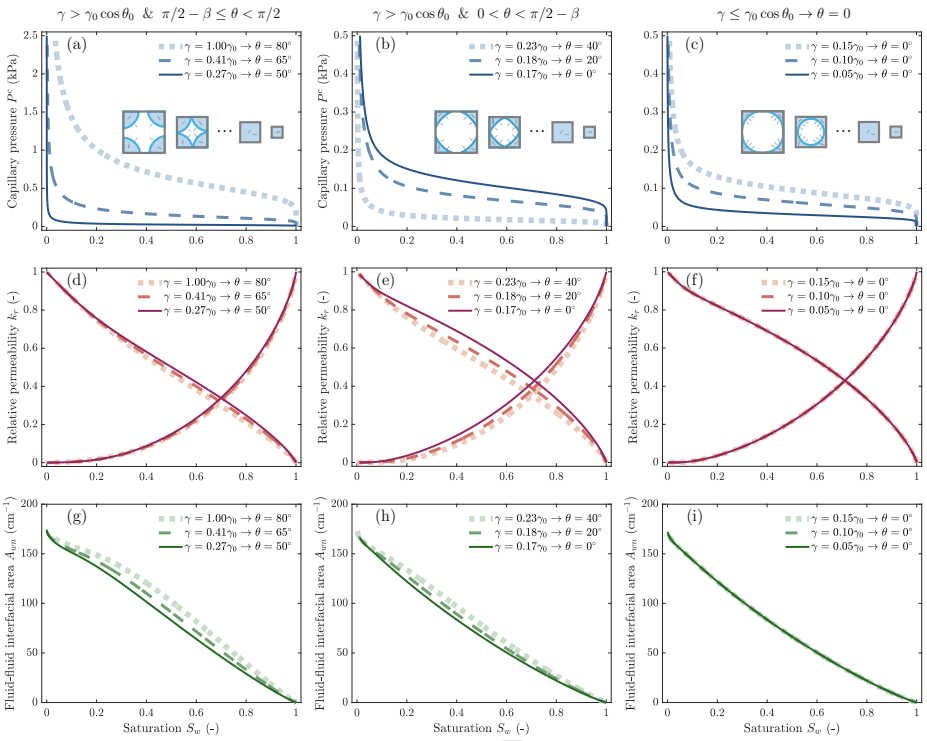

Figure 4: Impact of interfacial tension (γ_{wn}) on (a–c) capillary pressure–saturation curves, (e–f) relative permeability–saturation curves, and (g–i) fluid-fluid interfacial area–saturation curves in a porous medium with square-tube pores. A near neutral-wet condition (e.g., an intrinsic contact angle θ_0 of 80°) is used as an illustrative example. Three γ_{wn} ranges are examined: (1) A range within which the contact angles (θ) are greater than 0 and are equal or greater than $\pi/2 - \beta$, where β is the half corner angle and $\beta = \pi/4$ in the square tubes (left column), (2) A range where $0 < \theta < \pi/2 - \beta$ (middle column), and (3) A range where $\theta \equiv 0$ (right column). In the figure, $\gamma_{wn,0}$ refers to the interfacial tension for surfactant-free fluids. Note that γ_{wn} is a proxy of the surfactant effect, i.e., a smaller γ_{wn} corresponds to a more interfacially active surfactant and/or a higher surfactant concentration.

sensitive to the γ_{wn}-dependent convex vs. concave shapes of fluid menisci than r (Equations (13–14) and (16)).

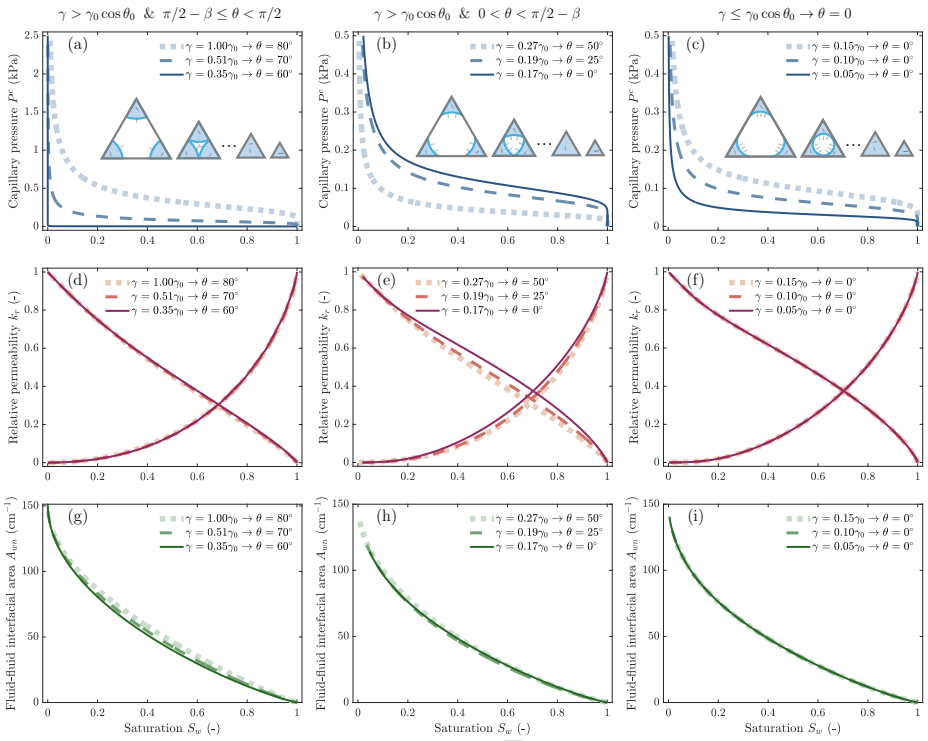

Figure 5: Impact of interfacial tension (γ_{wn}) on (a–c) capillary pressure–saturation curves, (e–f) relative permeability–saturation curves, and (g–i) fluid-fluid interfacial area–saturation curves in a porous medium with triangular-tube pores. A near neutral-wet condition (e.g., an intrinsic contact angle θ_0 of 80°) is used as an illustrative example. Three γ_{wn} ranges are examined: (1) A range within which the contact angles (θ) are greater than 0 and are equal or greater than $\pi/2 - \beta$, where β is the half corner angle and $\beta = \pi/6$ in the equilateral triangular tubes (left column), (2) A range where $0 < \theta < \pi/2 - \beta$ (middle column), and (3) A range where $\theta \equiv 0$ (right column). In the figure, $\gamma_{wn,0}$ refers to the interfacial tension for surfactant-free fluids. Note that γ_{wn} is a proxy of the surfactant effect, i.e., a smaller γ_{wn} corresponds to a more interfacially active surfactant and/or a higher surfactant concentration.

The γ_{wn}-dependent two-phase flow properties can strongly influence two-phase flow and surfactant transport behaviors in porous media with vary-

ing pore geometries. To capture these effects quantitatively, we incorporate the new properties into Darcy-scale transient two-phase flow and surfactant transport models (Section 2.5).

3.2. Validity and accuracy of simplified mathematical representations for two-phase flow properties

3.2.1. Numerical experiment design

To couple the γ_{wn}-dependent two-phase flow properties into Darcy-scale models, we have derived their explicit expressions and closed-form functions in Section 2.4. In this section, we evaluate the validity and accuracy of the explicit expressions and closed-form functions to ensure their reliability. This is achieved by comparing their predictions with those from the bundle-of-capillary-tubes model. Comparisons are performed for the three pore geometries at three representative surfactant concentrations (i.e., γ_{wn} values). Similarly, γ_{wn} is used as a proxy for the surfactant concentration—a larger γ_{wn} corresponds to a lower surfactant concentration. Here, the γ_{wn} values are chosen to capture the aforementioned two or three different regimes where the dependence of two-phase flow properties on pore annularity and γ_{wn} exhibits distinct behaviors (Section 3.1). For cylindrical pores, we use $\gamma/\gamma_{wn,0} = 0.22$, 0.10, and 0.05, corresponding to $\theta = 40°$, 0°, and 0°. For square-tube pores, we use $\gamma/\gamma_{wn,0} = 0.41$, 0.18, and 0.05, corresponding to $\theta = 65°$, 20°, and 0°. For equilateral triangular pores, we use $\gamma/\gamma_{wn,0} = 0.51$, 0.25, and 0.05, corresponding to $\theta = 70°$, 45°, and 0° (Note that angles are expressed in degrees (°) hereafter, unless otherwise specified). Two pore size distributions are examined: a more uniform pore size distribution where the mean and normalized standard deviation of the pore sizes are respectively 100 μm and 0.3 (i.e., the same as that in Section 3.1), and a wider pore size

distribution where the mean and normalized standard deviation of the pore sizes are respectively 100 μm and 0.5 (Figure B.1b).

3.2.2. Validation of explicit expressions and closed-form functions: Full lognormal pore size distribution

As shown in Figure 6, the explicit expressions fully overlap with the results from the bundle-of-capillary-tubes model in all the cases, which verifies the mathematical consistency between the explicit expressions and the bundle-of-capillary-tubes model. Similarly, the closed-form functions—which use a logistic function (i.e., $1/[1+\exp(-1.702x)]$) to approximate the cumulative normal distribution function (i.e., $\Phi(x)$) in the explicit expressions—align excellently with the bundle-of-capillary-tubes model. We observe a slight deviation in the fluid–fluid interfacial area–saturation (A_{wn}–S_w) curves at $S_w \to 1$. At $S_w \to 1$, most pores are unsaturated. The A_{wn} approximately scale with $1-\Phi(x)$ where $x = (\ln R_{\max} - \mu)/\sigma$ and $R_{\max} \to \infty$ with $R_{\max}$ being the maximum saturated pore size (Equations 24–26). Because the logistic function has a larger error at $x \to \infty$, $k_{r,w}$ and A_{wn} present a larger error at $R_{\max} \to \infty$ (i.e., $S_w \to 1$). In contrast, A_{wn} is near zero, and the corresponding fluid–fluid interfacial adsorption of surfactant is expected to be minor.

When the standard deviation of pore sizes increases to 0.5, both the explicit expressions and closed-form functions notably deviate from the bundle-of-capillary-tubes model (Figure D.3). This discrepancy is because the explicit expressions and closed-form functions cover the full range of a lognormal pore size distribution, while the bundle-of-capillary-tubes model can only approximate the lognormal pore size distribution by a truncated lognormal distribution.

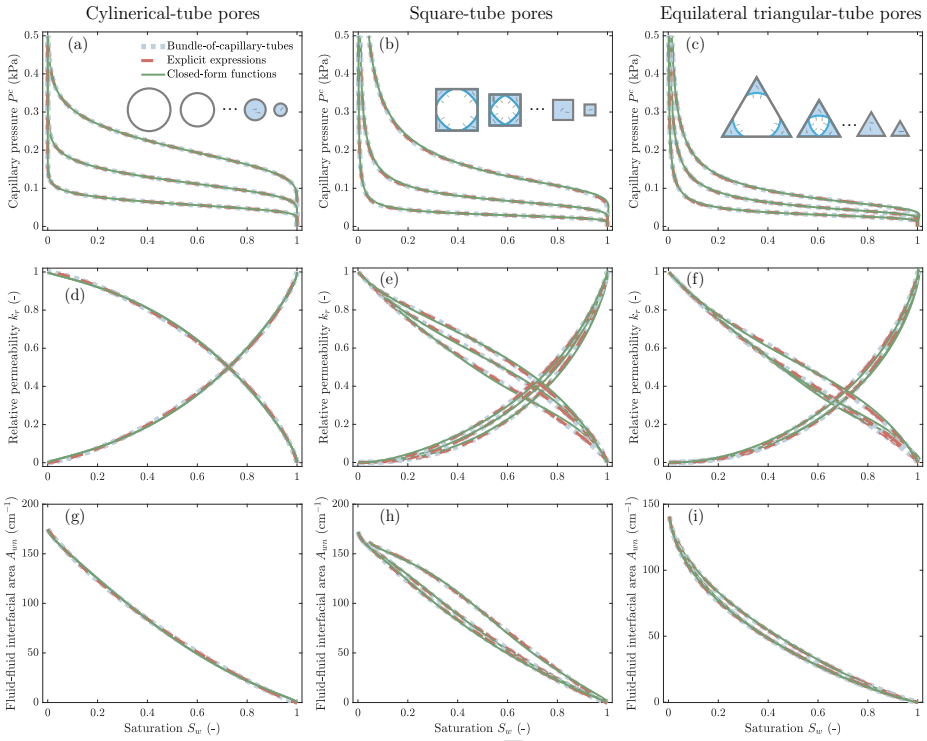

Figure 6: Evaluations on the explicit expressions and closed-form functions for (a–c) capillary pressure–saturation curves, (e–f) relative permeability–saturation curves, and (g–h) fluid-fluid interfacial area–saturation curves using the bundle-of-capillary-tubes model as a benchmark. Porous media with cylindrical, square-tube, and equilateral triangular-tube pores are examined. A near neutral-wet condition (e.g., an intrinsic contact angle of 80°) is used as an example. We present the curves at three example interfacial tensions (γ_{wn}) for each pore geometry—i.e., $\gamma_{wn}/\gamma_{wn,0} = 0.22$, 0.1, and 0.05 (i.e., $\theta = 40°$, 0° and 0°) for cylindrical pores; $\gamma_{wn}/\gamma_{wn,0} = 0.41$, 0.18, and 0.05 (i.e., $\theta = 65°$, 20° and 0°) for square-tube pores; and $\gamma_{wn}/\gamma_{wn,0} = 0.51$, 0.25, and 0.05 (i.e., $\theta = 70°$, 45° and 0°) for equilateral triangular-tube pores. The pore sizes follow a *full* lognormal distribution. The mean and normalized standard deviation of the pore sizes are respectively 100 μm and 0.3.

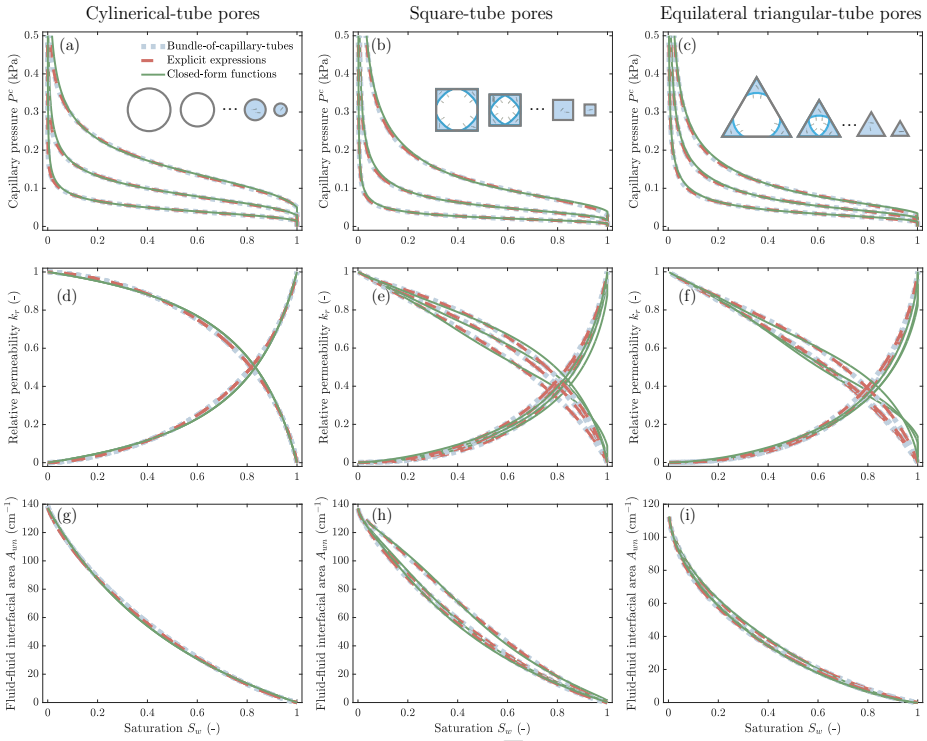

Figure 7: Evaluations on the explicit expressions and closed-form functions for (a–c) capillary pressure–saturation curves, (e–f) relative permeability–saturation curves, and (g–h) fluid-fluid interfacial area–saturation curves using the bundle-of-capillary-tubes model as a benchmark. Porous media with cylindrical, square-tube, and equilateral triangular-tube pores are examined. A near neutral-wet condition (e.g., an intrinsic contact angle of 80°) is used as an example. We present the curves at three example interfacial tensions (γ_{wn}) for each pore geometry—i.e., $\gamma_{wn}/\gamma_{wn,0}$ = 0.22, 0.1, and 0.05 (i.e., θ = 40°, 0° and 0°) for cylindrical pores; $\gamma_{wn}/\gamma_{wn,0}$ = 0.41, 0.18, and 0.05 (i.e., θ = 65°, 20° and 0°) for square-tube pores; and $\gamma_{wn}/\gamma_{wn,0}$ = 0.51, 0.25, and 0.05 (i.e., θ = 70°, 45° and 0°) for equilateral triangular-tube pores. The pore sizes follow a *truncated* lognormal distribution. The mean and normalized standard deviation of the pore sizes are 100 μm and 0.5, respectively; while the minimum and maximum pore sizes are 5 μm and 500 μm, respectively.

3.2.3. Validation of explicit expressions and closed-form functions: Truncated lognormal pore size distribution

To address the above discrepancy, we use a truncated lognormal pore size distribution (where the minimum and maximum pore sizes are 5 μm and 500 μm, respectively) to derive the closed-explicit expression and closed-form functions following the same procedure in Section 2.4. As shown in Figure 7, the explicit expressions overlap with the bundle-of-capillary-tubes model that applies the same truncated lognormal pore size distribution, verifying the mathematical consistency and accuracy between the two models. The closed-form functions have minor errors in calculating the capillary pressure and fluid–fluid interfacial area–saturation curves. However, the calculated relative permeability–saturation curves notably deviate from the reference curves, especially at $S_w \to 1$ where only a smaller amount of large pores are invaded by the nonwetting-phase fluid. The reason for this divination is the following. At $\sigma = 0.5$, the proportion of larger pores is greater than that at $\sigma = 0.3$. The invaded larger pores control the nonwetting-phase permeability and contribute a significant amount of wetting-phase permeability ($k_{nw} \propto R^4$). Additionally, the logistic function (i.e., $1/[1 + \exp(-1.702x)]$) makes larger errors at smaller or larger x. Collectively, the greater number of larger pores and a more significant error of the logistic function lead to a notable deviation.

Consequently, closed-formed functions are suggested for the capillary pressure–saturation curves of the two-phase flow models, while explicit expressions are recommended for the relative permeability–saturation curves. Either closed-form functions or explicit expressions can be employed for the interfacial area–saturation curves of the surfactant transport models, since

the interfacial area only enters the transport equation through surfactant mass balance and does not critically affect model structure.

3.3. Modeling coupled unsaturated water flow and PFAS transport in soils

The explicit expressions and closed-form functions are coupled into a Darcy-scale two-phase flow and surfactant transport (Section 2.5). Furthermore, the model is used to examine the impact of pore angularity and surfactant concentration on the coupled transient flow and transport processes for an example application, i.e., PFAS transport and leaching in soils. In particular, we simulate unsaturated water flow and PFAS transport through a vertical homogeneous soil column, which resembles a miscible displacement laboratory experiment (i.e., a laboratory experiment in which water containing a dissolved solute is injected into a soil column under constant infiltration conditions). The model employs the closed-form functions for the capillary pressure–saturation (P^c–S_w) curves, and the explicit expressions for the relative permeability (k_r) and fluid–fluid interfacial area–saturation (A_{wn}–S_w) curves. The details in the modeling setup and simulation results are presented below.

3.3.1. Numerical experiment design

We simulate the unsaturated water flow and PFAS transport behavior in the soil column using three versions of the model: (1) base case, which turns off the fluid–fluid interfacial adsorption of PFAS and its impact on interfacial tension (i.e., $\Gamma_{aw} = 0$ and $\gamma \equiv \gamma_0$, where Γ_{aw} is the air–water interfacial excess, γ is the surface tension for PFAS-laden water, γ_0 is the surface tension for PFAS-free water); (2) intermediate case, which turns on the fluid–fluid interfacial adsorption while keeping a constant γ (i.e., i.e.,

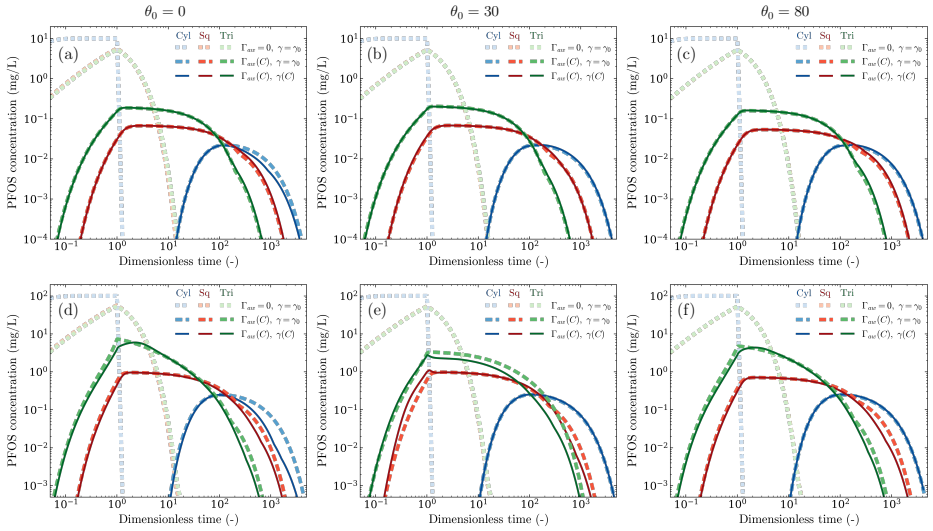

Figure 8: Impact of pore annularity, PFOS concentration, and intrinsic surface wettability on PFOS breakthrough curves in an unsaturated soil column. We consider two surface wettability: (a) completely water-wet ($\theta_0 = 0°$), (b) partially water-wet ($\theta_0 = 30°$), and (c) weakly water-wet ($\theta_0 = 80°$). For each surface wettability, we compare the PFOS breakthrough curves for three pore geometries: cylindrical tubes (denoted by "Cyl"), square tubes (denoted by "Sq"), and triangular tubes (denoted by "Tri"). The breakthrough curves are plotted on a log scale for both x and y axes. On the x-axis, the time is nondimensionalized by L/q, where L is the length of the soil column and q is the infiltration rate.

$\Gamma_{aw} = K_{aw}C$ and $\gamma \equiv \gamma_0$); (3) full model, which accounts for both the fluid–fluid interfacial adsorption of PFAS and its impact on γ (i.e., i.e., $\Gamma_{aw} = K_{aw}C$ and $\gamma = \gamma_0\,[1 - b\ln(1 + C/a)]$). Each model is applied to porous media with different pore geometries (cylindrical, square-tube, and equilateral triangular-tube) and intrinsic contact angles ($\theta_0 = 0°$, 30°, and 80°). We use PFOS as an example PFAS substance and simulate two representative aqueous concentrations (10 mg/L and 100 mg/L), yielding 18 total

simulations.

All simulations begin with a constant infiltration of PFOS-free water into a 10 cm-long dry soil column from the inlet (top), while the outlet (bottom) is maintained under free drainage. A small water saturation (0.001) is used to initiate the infiltration simulation. After the infiltration reaches the steady state, a pulse of PFAS solution (two pore volumes) is introduced at the same infiltration rate, with a zero concentration gradient imposed at the outlet. The parameters used for water flow and PFOS transport are summarized in the following: the infiltration rate is 0.42 cm/h, $\phi = 0.395\,\mathrm{cm}^3/\mathrm{cm}^3$, $k_0 = 1.19 \times 10^{-8}\,\mathrm{cm}^2$, $D_0 = 5.4 \times 10^{-6}\,\mathrm{cm}^2/\mathrm{s}$, $\mathcal{L}_w = 34.96\,\mathrm{cm}$, $\gamma_0 = 0.072\,\mathrm{N/m}$, $R_g = 8.314\,\mathrm{J/K/mol}$, $T = 293.15\,\mathrm{K}$, $a = 4{\times}10^{-3}\,\mathrm{mol/m}^3$, $b = 0.107$.

3.3.2. Unsaturated water flow and PFAS transport in soils

For each simulation, we compute the breakthrough curves at the outlet (Figure 8). As expected, PFOS shows significant retention due to adsorption at the air–water interface. However, the extent of retention varies strongly with pore geometry. The retardation factors (defined as the ratio of solute transport velocity to pore-water velocity) are approximately 306.5 for cylindrical pores, 6.6 for square-tube pores, and 3.0 for triangular-tube pores. This variation arises because pore geometry controls relative permeability and, in turn, water saturation under constant infiltration. Under steady infiltration of surfactant-free water, pore angularity alone leads to an order-of-magnitude difference in water saturation. As a result, the air–water interfacial areas differ markedly across geometries ($134.4\,\mathrm{cm}^{-1}$ for cylindrical pores, $48.6\,\mathrm{cm}^{-1}$ for square-tube pores, and $24.8\,\mathrm{cm}^{-1}$ for triangular-tube pores), which directly translates into an order-of-magnitude difference in retardation factors. These results highlight the critical role of pore geometry

in shaping two-phase flow properties—particularly relative permeability and air–water interfacial area—and thereby governing the transport of surface-active solutes such as PFAS.

As shown in Figure 8a–c, the models with and without accounting for interfacial tension variations produce nearly identical breakthrough curves for all three pore geometries at the lower concentration (10 mg/L), where the interfacial tension remains essentially unchanged. At the higher concentration (100 mg/L), the interfacial tension variations lead to a slight surfactant-induced flow and a slightly weaker retention (Figure 8d–f).

A close inspection of the soil column with cylindrical-tube pores and a contact angle of 30° shows that both interfacial tension and contact angle vary substantially in space and time. For an intrinsic contact angle of 30°, the simulations show that the interfacial tension decreases by up to 20% and the contact angle by as much as 30° (Figure 9c–d). These changes lead to a 30% reduction in water saturation in the upper soil and a 0.7% shift in water pressure head therein (Figure 9a–b). The fluctuations occur mainly in the top soils due to the strong retention and the resulting slower downward migration and spreading of PFOS across the soil column. Nevertheless, the greater relative permeability of cylindrical pores results in a lower water saturation and a larger air–water interfacial area at the same infiltration rate. This enlarged interfacial area promotes strong PFOS adsorption (Figure 9e), which in turn damps the fluctuations in water saturation and PFOS concentration induced by surfactant-driven flow. Therefore, the breakthrough curves only show a minor difference even at the higher concentration.

In soil columns with angular pores and an intrinsic contact angle of 30° (Figure 9h–i, m–n), the reductions in interfacial tension (<10%) and contact angle (< 15°) are much smaller. Correspondingly, water saturation varies

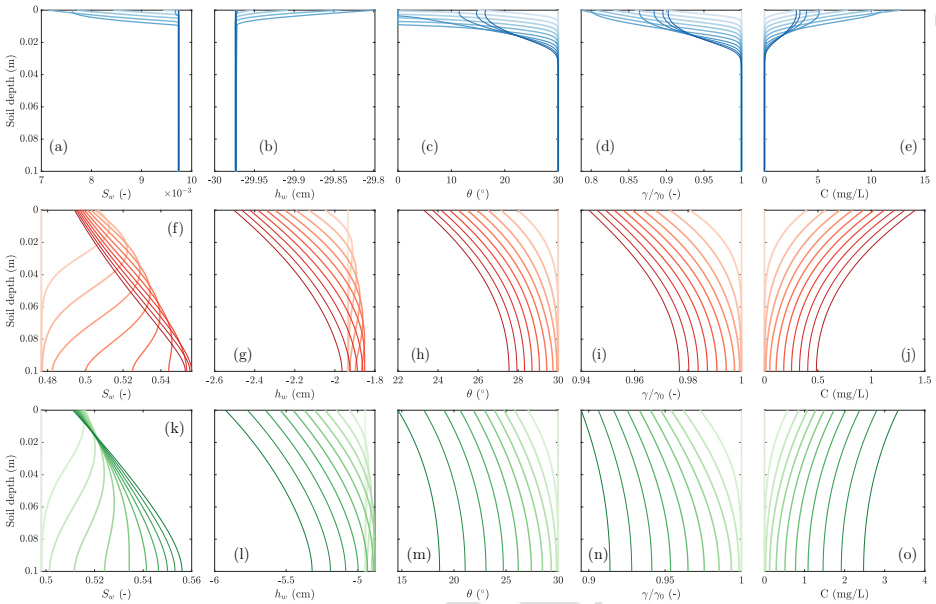

Figure 9: Temporal and spatial variations of water saturation (S_w), water pressure head (h_w), contact angle (θ), interfacial tension (γ, which is normalized by the interfacial tension for pure water γ_0), and aqueous PFOS concentration (C_{aq}) in an unsaturated soil column. We present the simulation results for all three pore geometries—including cylindrical tubes (top row), square tubes (middle row), and triangular tubes (bottom row)—at the PFOS concentration of 100 mg/L under partially water-wet condition ($\theta_0 = 30°$). We present the profiles from 0 to 4 hours at an interval of 0.4 hour for the porous medium with cylindrical pores, and those from 0 to 2 hours at an interval of 0.2 hour for the porous medium with angular pores. The lines become progressively darker to represent advancing simulation time.

by under 12% (Figure 9f&k). However, the water pressure head changes are more pronounced (about 44% for square-tube pores and 20% for triangular-tube pores) due to the weaker retention and thus faster downward migration and spreading of PFOS in the column (Figure 9g&l). To assess the role of the water pressure head changes, we compared the water pressure head

gradient with the gravitational force gradient across the entire domain. The computed gradients range from 0.08 to 0.12, which is much smaller than the gravitational gradient ($\partial h/\partial z = 1$, where h is the hydraulic head). Thus, the spatial variations in PFOS concentration, interfacial tension, and contact angle exert little influence on PFOS transport under these simulated conditions (Figure 9j&o).

In soils with intrinsic contact angles of 0° and 80°, the temporal and spatial variations of water saturation, pressure head, and contact angle slightly deviate from each other (Figures E.4 and E.5), due to the distinct dependence of capillary pressure–saturation curves on interfacial tension at different intrinsic contact angles. However, because of the insignificant surfactant-induced flow and strong retention, the PFOS concentration profiles present similar patterns as those in soils with an intrinsic contact angle of 30° (Figures E.4 and E.5). Correspondingly, the breakthrough curves are similar for different intrinsic contact angles, even at a higher concentration (100 mg/L).

4. Discussion

We present an upscaling workflow for simulating the coupled two-phase surfactant/PFAS-laden fluid flow and surfactant/PFAS transport in porous media with angular pores. The workflow derives REV-scale two-phase flow properties directly from pore-scale structural information (including intrinsic surface wettability, pore geometry, and pore-size distribution) and surfactant chemistry conditions. These REV-scale properties are then coupled into a transient two-phase flow and surfactant/PFAS transport model, enabling prediction of complex flow and transport behaviors across a wide range of porous media using only a minimal set of pore-scale structural parameters.

The approach offers a practical tool for applications such as contaminant transport and remediation (e.g., NAPL and PFAS) in soils and groundwater (e.g., Al-Raoush, 2009; Guo et al., 2020; Maroli et al., 2024).

4.1. New scaling functions for two-phase flow properties of surfactant-laden fluids in porous media

Through modeling investigations, we identify new scaling functions for the two-phase flow properties of surfactant-laden fluids in porous media, distinct from the classic Leverett J-function (Leverett, 1941) and its modified forms (e.g., Rose and Bruce, 1949; Lan et al., 2025). The Leverett J-type scalings extrapolate the capillary pressure–saturation (P^c–S_w) curve of a given rock and surfactant-free fluid system to other rocks or fluid pairs by normalizing with $1/(\gamma_{wn,0}\cos\theta_0)$ or $1/(\gamma_{wn,0}f(\theta_0))$, where $\gamma_{wn,0}$ is the interfacial tension for surfactant-free fluids, θ_0 is the intrinsic contact angle, and f is a function of θ_0. For surfactant-laden fluids, a common empirical extension is to substitute $\gamma_{wn,0}$ and θ_0 with γ_{wn} and θ, where γ_{wn} and θ are treated as independent empirical or semi-empirical functions of surfactant type and concentration (e.g., Bhattacharjee et al., 2025). However, as implied by the Young–Dupré equation, γ_{wn} and θ are coupled. Our scaling functions, derived mechanistically from the Young–Dupré relation and the bundle-of-capillary-tubes model, take into account this coupling effect. They yield two-phase flow properties only depending on γ_{wn} (i.e., surfactant types and concentrations) and pore structures.

Additionally, most previous studies adopted a linear Leverett J-type scaling of the P^c–S_w curve and assumed invariant K_r–S_w and A_{wn}–S_w curves. In contrast, our scaling functions predict a piecewise linear relationship between P^c–S_w and γ_{wn} in porous media with cylindrical pores, and a mono-

tonic, nonlinear relationship in porous media with angular pores. Furthermore, the relative permeability–saturation (K_r–S_w) and fluid–fluid interfacial area–saturation (A_{wn}–S_w) curves both vary with γ_{wn}. The new scaling functions may capture more realistic two-phase flow behaviors of surfactant-laden fluids in porous media with diverse geometries. Incorporating these new properties into Darcy-scale models is essential for accurately predicting transient two-phase flow and contaminant transport in porous media, particularly under conditions where surfactant effects are significant.

4.2. Experimental validation of the proposed scaling functions

To validate the proposed scaling functions, we compare the model predictions against experimentally measured capillary pressure–saturation curves of surfactant(Triton X-100)-laden fluids in an F-70 Ottawa sand (Karagunduz et al., 2001). The comparison involves two steps: (1) We compute the pore size distribution using the van Genuchten (VG) curve fitting best with the experimentally measured capillary pressure–saturation curve of surfactant-free fluids. Specifically, we can compute the cumulative density function of the pore sizes via $F_{\mathrm{V}}(R_{\max}) = S_{w,\mathrm{VG}}(P^c) = S_{w,\mathrm{VG}}(P^c(R_{\max}))$, where F_{V} is the cumulative volume of pores whose sizes are below $R_{\max}$, $S_{w,\mathrm{VG}}(P^c)$ is the VG model, $P^c(R_{\max})$ is given by the bundle-of-capillary-tubes model (Equation (17)) or its simplified expressions with $\gamma = \gamma_0$ and $\theta = \theta_0$, and $R_{\max}$ is the maximum pore size below which the pores remain fully occupied by the wetting-phase fluid. Consequently, the probability density function of the pore sizes is given by $f_{\mathrm{V}}(R_{\max}) = \frac{\mathrm{d}F_{\mathrm{V}}(R_{\max})}{\mathrm{d}R_{\max}} = \frac{\mathrm{d}S_{w,\mathrm{VG}}(P^c)}{\mathrm{d}P^c}\frac{\mathrm{d}P^c(R_{\max})}{\mathrm{d}R_{\max}}$, where f_{V} represents the volume of pores with radius $R_{\max}$. We can divide f_{V} by the volume of a single pore to yield the corresponding pore count. (2) We predict the capillary pressure–saturation curves

of surfactant-laden fluids using the derived pore size distribution and measured interfacial properties (γ and θ) on planar slides made of the same material as that of the studied porous medium, and compare the predictions with their corresponding experimentally measured capillary pressure–saturation curves. To minimize the occurrence and influence of more complex two-phase flow processes (e.g., trapping and hysteresis), the validation is done using experimental measurements during primary drainage. The specifics are provided below.

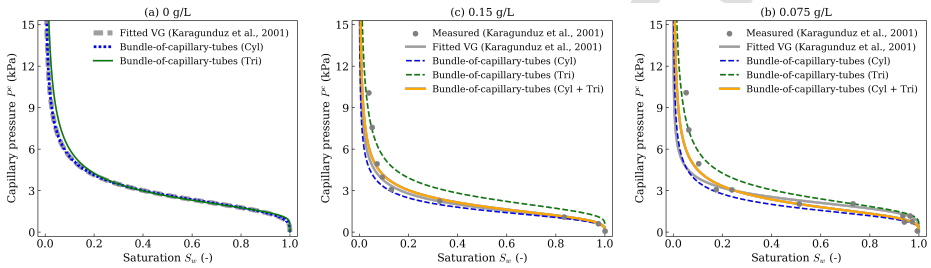

Figure 10: Experimental validation of the new scaling functions for two-phase flow properties of surfactant(Triton X-100)-laden fluids in an F-70 Ottawa sand (Karagunduz et al., 2001). (a) Derivation of pore size distribution from the van Genuchten (VG) curve of surfactant-free fluids and validation of bundle-of-capillary-tubes models using cylindrical tubes (denoted by "Cyl") or triangular tubes (denoted by "Tri"). (b–c) Validation of predicted capillary pressure–saturation curves for surfactant-laden fluids using the derived pore size distribution at two Triton X-100 concentrations: 0.075 g/L and 0.15 g/L. The predictions are provided by bundle-of-capillary-tubes models with three different pore geometries, including cylindrical tubes (denoted by "Cyl"), triangular tubes (denoted by "Tri"), and a combination of cylindrical and triangular tubes (denoted by "Cyl + Tri"). All VG curves were obtained by fitting with experimental data and the VG parameters were reported by Karagunduz et al. (2001).

We use cylindrical and triangular tubes to approximate the rounded to sub-angular pore spaces in the F-70 Ottawa sand (e.g., Bastidas, 2016). As

shown in Figure 10a, the bundle-of-capillary-tubes models using the VG curve-derived pore size distributions and measured interfacial properties (γ_0 and θ_0, see Table F.1) accurately reproduce the experimental data-fitted VG curve for surfactant-free fluids (Karagunduz et al., 2001), verifying the theoretical derivation of pore size distributions. The same models are used to predict the capillary pressure–saturation curves of surfactant-laden fluids using measured interfacial properties (γ and θ, see Table F.1) on quartz slides at two concentrations (i.e., 0.075 g/L and 0.15 g/L). We observe that the model using cylindrical tubes consistently overestimates the reduction of capillary pressure by surfactants, the one using triangular tubes shows the opposite (Figure 10b–c). These deviations may be caused by the coexistence of rounded and sub-angular pore spaces in the F-70 Ottawa sand. To account for this phenomena, we further estimate the curve via a weighted average of the two models, i.e., $S_w(P^c) = W \cdot S_{w,\mathrm{Cyl}}(P^c) + (1-W) \cdot S_{w,\mathrm{Tri}}(P^c)$ where W is the volume fraction of cylindrical pores, and the subscripts "Cyl" and "Tri" represents the models using cylindrical and triangular tubes, respectively. Interestingly, the weighted average significantly improves the accuracy of the predictions at a wide range of W (i.e., $W = 0.55 \sim 1.00$). For example, with $W = 0.65$, the root mean square errors between the predictions and measurements decrease from 0.128 (cylindrical tubes) and 0.104 (triangular tubes) to 0.079 (weighted average) at 0.075 g/L, while decreasing from 0.040 (cylindrical tubes) and 0.126 (triangular tubes) to 0.028 (weighted average) at 0.15 g/L. These errors are also close to the errors of the VG curves that were best fitted to the measurements (0.059 at 0.075 g/L and 0.020 at 0.15 g/L). Both the error reduction and the good match validate the predictive capability of the bundle-of-capillary-tubes models and the accuracy of the new scaling functions.

More importantly, the above analyses suggest that, through an appropriate approximation of pore geometry and pore size distribution, the simplified bundle-of-capillary-tubes models can provide good predictions for the capillary pressure-saturation curves and potential other two-phase flow properties of surfactant-laden fluids in real porous media using minimal experimental measurements (i.e., capillary pressure-saturation curves of surfactant-free fluids and interfacial properties of surfactant-laden fluids on planar slides of the same solid materials).

4.3. Coupling of new two-phase flow properties into transient two-phase flow and surfactant transport model

We acknowledge that many prior studies have derived two-phase flow properties for surfactant-free fluids by accounting for factors such as thin fluid films, pore geometry, surface wettability, and surface roughness (e.g., Tuller et al., 1999; Diamantopoulos and Durner, 2013; Bhattacharjee et al., 2025), and have proposed explicit expressions or closed-form functions for these properties (e.g., Diamantopoulos and Durner, 2015). However, to our knowledge, these developments have rarely been carried through into transient two-phase flow and transport models, even for surfactant-free fluid systems. This gap likely stems from the analytical complexity of the derived relationships, the absence of simplified forms suitable for numerical implementation, and/or the additional challenges of coupling them with nonlinear two-phase flow and transport processes.

Here, we for the first time demonstrate the feasibility of coupling theoretically derived properties for surfactant-laden fluids and their simplified expressions into a transient two-phase flow and transport framework. The coupled model is solved using either a fully implicit or a sequentially im-

plicit scheme, with preliminary tests suggesting that the sequentially implicit method offers superior numerical stability. While further investigation is needed to address the mathematical complexity and to develop more robust numerical algorithms, our example simulations of unsaturated water flow and PFAS (surfactant-like chemical) transport show that the model successfully captures both water flow fluctuations and PFAS transport dynamics in unsaturated soils. These findings demonstrate that the approach is not only theoretically sound but also practically feasible, paving the way for broader applications in coupled two-phase flow and surfactant transport systems

4.4. Implications for PFAS transport in vadose zone soils

Furthermore, the PFAS transport simulations show that PFAS migration and retention in unsaturated soils are strongly governed by pore geometry. Simulations under constant infiltration rates reveal sharp contrasts among pore types: cylindrical pores yield retardation factors on the order of 300, compared to 6.6 and 3.0 for square and triangular pores, respectively. This variation arises primarily from differences in water saturation and interfacial area under simulated infiltration conditions. Cylindrical pores maintain low saturation and large interfacial areas, conditions favorable for strong PFOS adsorption. In contrast, angular pores sustain higher saturation and smaller interfacial areas, leading to weaker retention. These findings suggest that soils dominated by cylindrical-like pores (if they exist) may act as long-term PFAS reservoirs, whereas soils with more angular pores may facilitate faster contaminant migration. This distinction highlights the importance of considering pore geometry in predicting PFAS transport and designing targeted remediation strategies.

In contrast to pore geometry, the simulations indicate that surfactant-induced flow has a subtle impact on PFAS (e.g., PFOS) transport. This finding is consistent with miscible displacement experiments conducted with both PFAS and non-PFAS surfactants at similar concentration levels (Brusseau et al., 2007, 2015; El Ouni et al., 2021). At the field scale, however, the extent of surfactant-induced flow and its influence on PFAS transport remains unsettled. For example, Zeng and Guo (2021) observed similar vertical concentration profiles between long-term one- and two-dimensional simulations for PFAS concentrations up to 1,000 mg/L, concluding that surfactant-induced flow was negligible. In contrast, other studies suggest that surfactant-induced flow can play a more significant role in the lateral spreading of bulk aqueous fire-fighting foam at orders-of-magnitude higher concentrations, but without considering vertical flow and transport processes (Valvatne et al., 2005). These differences appear to depend strongly on PFAS type and concentration level, flow and transport representation (e.g., vertical vs. lateral vs. full two-/three-dimensional), as well as site-specific conditions such as infiltration rates and soil heterogeneity. To explore these factors, a two-/three-dimensional form of our model or other existing two-/three-dimensional models (e.g., Zeng and Guo, 2021) can be applied.

We recognize that the presented simulations focus on short-term PFAS transport within a shallow ($\sim$10 cm) soil column. The results are intended to elucidate fundamental pore-scale mechanisms rather than to directly predict long-term field-scale behavior. The relevance of these mechanisms to deeper vadose-zone soils (>1 m) and longer time scales—where PFAS leaching poses the greatest risk to groundwater—remains an open question. Addressing this gap will require future studies that link pore-scale retention and mass-transfer parameters to depth-resolved vadose-zone models, thereby en-

abling the evaluation of cumulative PFAS leaching and mass discharge under realistic meteorological and hydrologic forcing.

Finally, we note that while most prior PFAS transport studies applied a simplified two-phase flow model (i.e., Richards' equation) to focus on transport in a single fluid such as water (e.g., Guo et al., 2020; Silva et al., 2020), our model—a generalization of Richards' equation—accounts for full two-phase flow and PFAS transport in both air and water. This broader framework is particularly useful for representing systems where PFAS transport and mass transfer in both phases are significant. For example, volatile PFAS compounds require modeling transport in both air and water (e.g., Brusseau and Guo, 2024), and similar considerations apply to water–NAPL systems with substantial PFAS partitioning into both phases (e.g., Liao et al., 2022). These advancements mark a critical step toward accurate long-term leaching predictions, site-specific risk assessments, and the design of effective remediation strategies in complex environmental settings.

4.5. Model limitations and extensions

While the model in this study adopts several simplifying assumptions—idealized pore geometry, lognormal or truncated lognormal pore size distribution, and uniform wettability, it can be extended to more complex conditions. Potential extensions include broader classes of angular pore geometries, multimodal pore size distributions, and mixed-wet porous media. For additional angular geometries beyond square and triangular tubes, the two-phase flow properties and their simplified mathematical forms can be derived using the methodology in Section 2. In the case of a multimodal pore size distribution, the problem can be decomposed into a superposition of multiple single-modal distributions, with properties derived for each mode and then

combined. For mixed-wet porous media, effective two-phase properties can be obtained by superposing contributions from pores of different intrinsic contact angles. These extensions will broaden the applicability of the framework to diverse surfactant-laden flow and porous media systems, including biosurfactant–water-soil environments (Yang et al., 2021; Li et al., 2022), oil and gas reservoirs (Lake, 1989), and geological CO_2/H_2 storage formations (Føyen et al., 2020; Chaturvedi et al., 2022).

The bundle-of-capillary-tubes model necessarily simplifies pore structure by neglecting spatial connectivity and arrangement. It may not capture some additional pore-scale phenomena (e.g., fluid trapping and hysteresis during cyclic drainage–imbibition experiments) under certain experimental and field conditions. When such processes are important, more realistic pore-scale models—such as pore morphology model (e.g., Hazlett, 1995; Hilpert and Miller, 2001), pore-network model (e.g., Fatt, 1956; Reeves and Celia, 1996; Chen and Guo, 2023), and direct numerical simulations (e.g., Martys and Chen, 1996; Raeini et al., 2012)—can be employed to derive two-phase properties. However, these approaches often do not yield closed-form analytical expressions, creating challenges for direct coupling with Darcy-scale models. In such cases, we can embed advanced pore-scale models (e.g., pore networks) directly within each grid block of a Darcy-scale model and form a multiscale framework (e.g., Blunt et al., 2002). Another practical and computationally efficient approach is employing empirical fitting to obtain tractable functions for Darcy-scale simulations. These developments hold promise for improving the predictive capability and accuracy of field-scale simulations under real-world conditions.

5. Conclusion

We present an upscaling workflow to quantify how pore-scale variations in surfactant/PFAS-associated interfacial properties (i.e., interfacial tension and contact angle) and pore angularity influence Darcy-scale two-phase flow and surfactant/PFAS transport. The workflow proceeds through four key steps: (1) Compute the fluid–fluid configuration in nonangular or angular pores for a given capillary pressure and interfacial tension (i.e., surfactant/PFAS type and concentration), (2) Determine fluid–fluid partitioning in a bundle of capillary tubes at the specified capillary pressure, (3) Derive two-phase flow properties (e.g., capillary pressure, relative permeability, and fluid–fluid interfacial area as functions of saturation) using the bundle-of-capillary-tubes model, (4) Couple these properties into Darcy-scale transient two-phase flow and surfactant/PFAS transport models. This pore-scale to Darcy-scale upscaling workflow provides a mechanistic tool to study the complex interactions between transient two-phase flow and surfactant/PFAS transport processes in diverse porous media.

Our modeling investigations suggest a nonmonotonic and/or nonlinear dependence of two-phase flow properties on the interfacial tension (or surfactant/PFAS type and concentration) and pore structures (i.e., pore geometry and size distribution). These new two-phase flow properties are validated by a close match between model predicted and experimentally measured capillary pressure-saturation curves for surfactant-laden fluids in real porous media samples (e.g., quartz sands). Furthermore, these two-phase flow properties is coupled into a general two-phase flow model for simulating the transport of example surfactant-like contaminant (PFAS) transport through unsaturated soil columns (e.g., the shallow soil layer of the vadose

zone). The model simulations reveal that PFAS downward migration is significantly delayed in unsaturated soils with cylindrical pores by the lower water saturation and higher air–water interfacial area, whereas angular pores enhance PFAS retention by increasing the water saturation and decreasing the air–water interfacial area. The findings highlight the critical role of pore angularity on PFAS retention behaviors.

Beyond the demonstrated PFAS systems, this framework provides a generalizable tool for bridging pore-scale physics and continuum-scale modeling to support predictions and management of multiphase systems in environmental and energy contexts, with potential applications in contaminant transport, enhanced oil recovery, underground CO_2/H_2 storage, and othe relevant problems.

6. Acknowledgment

The authors thank Mr. Wenqian Zhang and Ms. Shujie Guo at the University of Arizona for the discussion on the PFAS-modified interfacial tension and contact angle in a single pore.

Appendix A. Permeability of fluid in a half corner of an angular pore

The dimensionless conductance of the wetting phase at the i^{th} half corner $\tilde{g}_{\alpha,i}$ given by

$$\tilde{g}_{\alpha,i} = \exp\left(\frac{m_1\tilde{G}_{\alpha,i}^2 + m_2\tilde{G}_{\alpha,i} + m_3 + 0.02\sin(\beta_i - \pi/6)}{1/4/\pi - \tilde{G}_{\alpha,i}} + 2\ln\tilde{A}_{\alpha,i}\right), \tag{A.1}$$

where $m_1 = -18.2066$, $m_2 = 5.88287$, and $m_3 = -0.351809$ are fitting parameters (Patzek and Kristensen, 2001), $\tilde{A}_{\alpha,i}$ and $\tilde{G}_{\alpha,i}$ are the area and

shape factor of the wetting-phase region at a corner with a unit meniscus-apex distance (i.e., $l_{\alpha,i} = 1$), respectively. $\tilde{A}_{\alpha,i}$ is given by

$$\tilde{A}_{\alpha,i} = \left[\frac{\sin\beta_i}{\cos(\theta+\beta_i)}\right]^2 \left[\frac{\cos\theta\cos(\theta+\beta_i)}{\sin\beta_i} + \theta + \beta_i - \frac{\pi}{2}\right], \tag{A.2}$$

and $\tilde{G}_{\alpha,i}$ is given by

$$\tilde{G}_{\alpha,i} = \frac{\tilde{A}_{\alpha,i}}{4\left[1-(\theta+\beta_i-\pi/2)\sin\beta_i/\cos(\theta_i+\beta)\right]^2}. \tag{A.3}$$

Appendix B. Pore size distributions

Figure B.1 shows the pore size distributions for the two porous media simulated in Sections 3.1 and 3.2.

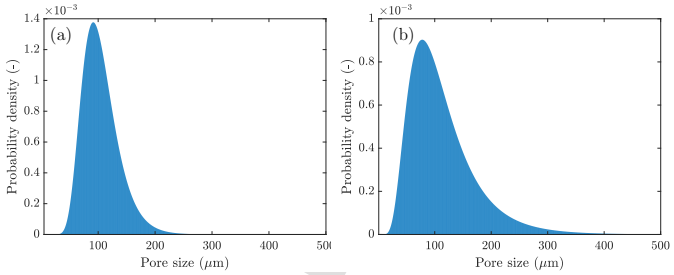

Figure B.1: Pore size distributions of porous media with (a) a mean pore size of 100μm and normalized standard deviation of 0.3, and (b) a mean pore size of 100μm and normalized standard deviation of 0.5.

Appendix C. Relative permeability and fluid–fluid interfacial area as functions of saturation in porous media with cylindrical pores

Figure C.2 presents the relative permeability and fluid–fluid interfacial area as functions of saturation in the porous medium with cylindrical pores simulated in 3.1.

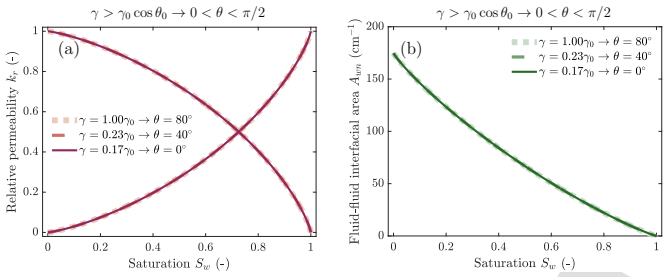

Figure C.2: Impact of interfacial tension (γ_{wn}) on the relative permeability and fluid–fluid interfacial area as functions of saturation in porous media with cylindrical pores. A near neutral-wet condition (e.g., an intrinsic contact angle θ_0 of 80°) is used as an illustrative example.We present the curves for the γ_{nw} range where the contact angles become 0 and remain constant. Note that γ_{wn} is a proxy of the surfactant effect, i.e., a smaller γ_{wn} corresponds to a more interfacially active surfactant and/or a higher surfactant concentration.

Appendix D. Accuracy of the explicit expressions and closed-form functions

Figure D.3 presents the evaluations of explicit expressions and closed-form functions for the two-phase flow properties by comparing with the bundle-of-capillary-tubes model.

Appendix E. Temporal and spatial variations of flow and transport variables

Appendix F. Parameters for experimental validation

References

Abriola, L.M., Dekker, T.J., Pennell, K.D., 1993. Surfactant-enhanced solubilization of residual dodecane in soil columns. 2. Mathematical modeling. Environmental Science & Technology 27, 2341–2351.

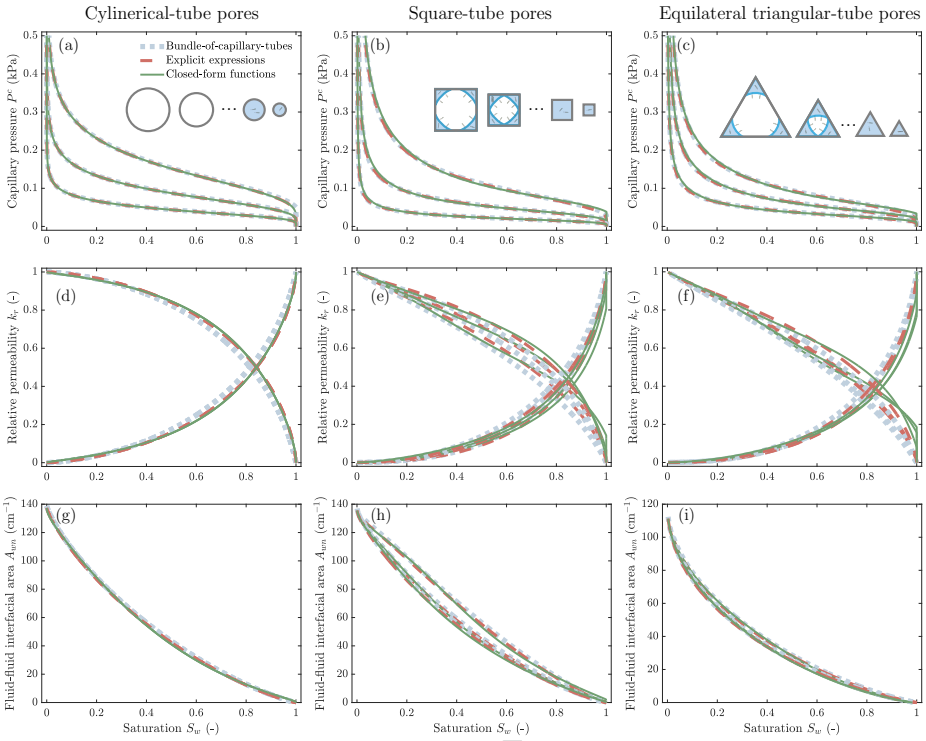

Figure D.3: Evaluations on the explicit expressions and closed-form functions for (a–c) capillary pressure–saturation curves, (e–f) relative permeability–saturation curves, and (g–h) fluid-fluid interfacial area–saturation curves using the bundle-of-capillary-tubes model as a benchmark. Porous media with cylindrical, square-tube, and equilateral triangular-tube pores are examined. A near neutral-wet condition (e.g., an intrinsic contact angle of 80°) is used as an example. We present the curves at three example interfacial tensions (γ_{wn}) for each pore geometry—i.e., $\gamma_{wn}/\gamma_{wn,0} = 0.22$, 0.1, and 0.05 (i.e., $\theta = 40°$, 0° and 0°) for cylindrical pores; $\gamma_{wn}/\gamma_{wn,0} = 0.41$, 0.18, and 0.05 (i.e., $\theta = 65°$, 20° and 0°) for square-tube pores; and $\gamma_{wn}/\gamma_{wn,0} = 0.51$, 0.25, and 0.05 (i.e., $\theta = 70°$, 45° and 0°) for equilateral triangular-tube pores. A lognormal pore size distribution is used. The mean and normalized standard deviation of the pore sizes are 100 μm and 0.5, respectively.

Al-Raoush, R.I., 2009. Impact of wettability on pore-scale characteristics of residual nonaqueous phase liquids. Environmental Science & Technology

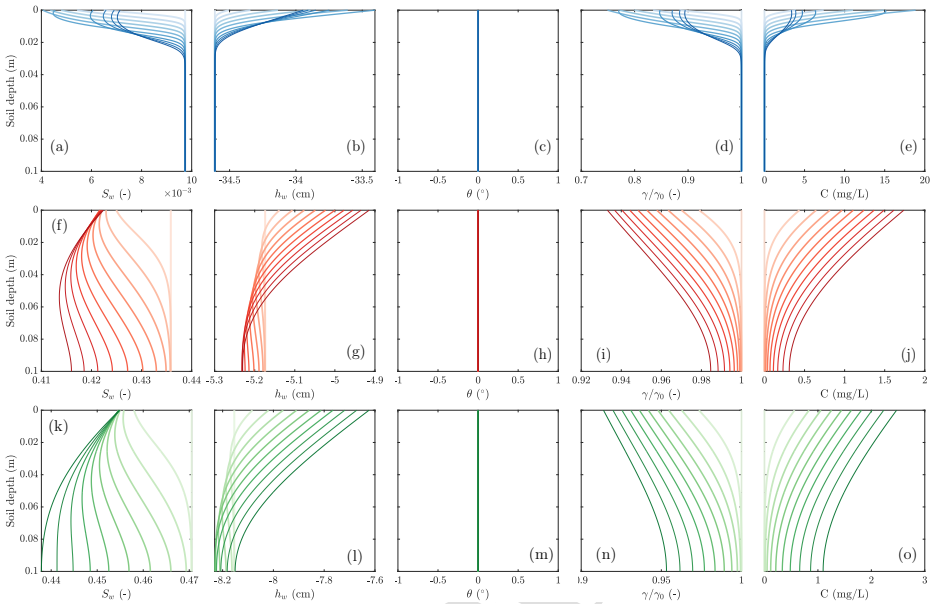

Figure E.4: Temporal and spatial variations of water saturation (S_w), water pressure head (h_w), contact angle (θ), interfacial tension (γ, which is normalized by the interfacial tension for pure water γ_0), and aqueous PFOS concentration (C_{aq}) in an unsaturated soil column. We present the simulation results for all three pore geometries—including cylindrical tubes (top row), square tubes (middle row), and triangular tubes (bottom row)—at the PFOS concentration of 100 mg/L under completely water-wet condition ($\theta_0 = 0°$). We present the profiles from 0 to 4 hours at an interval of 0.4 hour for the porous medium with cylindrical pores, and those from 0 to 2 hours at an interval of 0.2 hour for the porous medium with angular pores. The lines become progressively darker to represent advancing simulation time.

43, 4796–4801.

Bastidas, A.M.P., 2016. Ottawa F-65 sand characterization. University of California, Davis.

Bhattacharjee, D., Ramon, G.Z., Edery, Y., 2025. The evolution of invasion

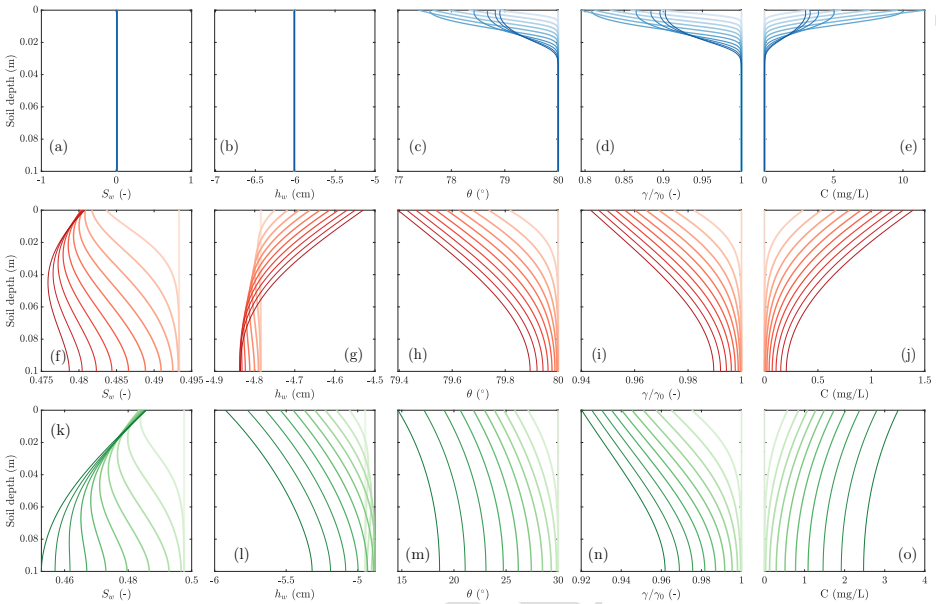

Figure E.5: Temporal and spatial variations of water saturation (S_w), water pressure head (h_w), contact angle (θ), interfacial tension (γ, which is normalized by the interfacial tension for pure water γ_0), and aqueous PFOS concentration (C_{aq}) in an unsaturated soil column. We present the simulation results for all three pore geometries—including cylindrical tubes (top row), square tubes (middle row), and triangular tubes (bottom row)—at the PFOS concentration of 100 mg/L under weakly water-wet condition ($\theta_0 = 80°$) . We present the profiles between 0 and 4 hours at an interval of 0.4 hour for the porous medium with cylindrical pores, and those between 0 and 2 hours at an interval of 0.2 hour for the porous medium with angular pores. The lines become progressively darker to represent advancing simulation time.

patterns due to surfactant adsorption in anomalous pore distribution: Role of mass transfer and Laplace pressure. arXiv preprint arXiv:2505.13464 .

Blunt, M.J., Jackson, M.D., Piri, M., Valvatne, P.H., 2002. Detailed physics, predictive capabilities and macroscopic consequences for pore-network models of multiphase flow. Advances in Water Resources 25, 1069–1089.

Table F.1: Van Genuchten (VG) model parameters for deriving the pore size distribution of F-70 Ottawa sand (θ_r, θ_s, n, and α_{VG}) and parameters predicting capillary pressure-saturation curves of surfactant-laden fluids. All the parameters were reported in the work of Karagunduz et al. (2001). Note that the VG parameters for a surfactant concentration of 0.075 g/L were mistakenly assigned to 0.050 g/L in the origianl reference. The corrected values for 0.075 g/L are provided here.

Surfactant concentration	Parameter	Unit	Value
0 g/L	θ_s	$\mathrm{cm}^3/\mathrm{cm}^3$	0.3520
	θ_r	$\mathrm{cm}^3/\mathrm{cm}^3$	0.00008
	n	-	3.6762
	α_{VG}	Pa^{-1}	4.1966
	γ	N/m	0.072
	θ	°	40.7
0.075 g/L	θ_s	$\mathrm{cm}^3/\mathrm{cm}^3$	0.3570
	θ_r	$\mathrm{cm}^3/\mathrm{cm}^3$	0.00008
	n	-	4.5561
	α_{VG}	Pa^{-1}	4.7688
	γ	N/m	0.0379
	θ	°	16.2
0.15 g/L	θ_s	$\mathrm{cm}^3/\mathrm{cm}^3$	0.3495
	θ_r	$\mathrm{cm}^3/\mathrm{cm}^3$	0.00007
	n	-	3.6070
	α_{VG}	Pa^{-1}	6.0542
	γ	N/m	0.0335
	θ	°	13.1

Brusseau, M.L., El Ouni, A., Araujo, J.B., Zhong, H., 2015. Novel methods for measuring air–water interfacial area in unsaturated porous media. Chemosphere 127, 208–213.

Brusseau, M.L., Guo, B., 2024. Vapor-phase transport of per and polyfluoroalkyl substances: Processes, modeling, and implications. Science of the Total Environment 947, 174644.

Brusseau, M.L., Peng, S., Schnaar, G., Murao, A., 2007. Measuring air- water

interfacial areas with x-ray microtomography and interfacial partitioning tracer tests. Environmental Science & Technology 41, 1956–1961.

Chaturvedi, K.R., Bajpai, S., Trivedi, J., Sharma, T., 2022. Air foams for mobility control and subsurface storage of hydrogen in porous media: an experimental study. Energy & Fuels 36, 5036–5046.

Chen, S., Guo, B., 2023. Pore-scale modeling of PFAS transport in water-unsaturated porous media: Air–water interfacial adsorption and mass-transfer processes in thin water films. Water Resources Research 59, e2023WR034664.

Chen, S., Qin, C., Guo, B., 2020. Fully implicit dynamic pore-network modeling of two-phase flow and phase change in porous media. Water Resources Research 56, e2020WR028510.

Desai, F., Demond, A., Hayes, K., 1991. The influence of surfactant sorption on capillary pressure-saturation relationships. Technical Report. Michigan Univ., Ann Arbor, MI (United States). Dept. of Civil and Environmental Engineering.

Diamantopoulos, E., Durner, W., 2013. Physically-based model of soil hydraulic properties accounting for variable contact angle and its effect on hysteresis. Advances in Water Resources 59, 169–180.

Diamantopoulos, E., Durner, W., 2015. Closed-form model for hydraulic properties based on angular pores with lognormal size distribution. Vadose Zone Journal 14, vzj2014–07.

Dong, M., Chatzis, I., 1995. The imbibition and flow of a wetting liquid along

the corners of a square capillary tube. Journal of Colloid and Interface Science 172, 278–288.

Dullien, F.A., 2012. Porous media: fluid transport and pore structure. Academic press.

Dupré, A., Dupré, P., 1869. Théorie mécanique de la chaleur. Gauthier-Villars.

El Ouni, A., Guo, B., Zhong, H., Brusseau, M.L., 2021. Testing the validity of the miscible-displacement interfacial tracer method for measuring air-water interfacial area: Independent benchmarking and mathematical modeling. Chemosphere 263, 128193.

Fatt, I., 1956. The network model of porous media. Transactions of the AIME 207, 144–181.

Føyen, T., Brattekås, B., Fernø, M., Barrabino, A., Holt, T., 2020. Increased CO_2 storage capacity using CO_2-foam. International Journal of Greenhouse Gas Control 96, 103016.

Ge, W., Chen, Y., Fan, Y., Zhu, Y., Liu, H., Song, L., Liu, Z., Lian, C., Jiang, H., Li, C., 2022. Dynamically formed surfactant assembly at the electrified electrode–electrolyte interface boosting CO_2 electroreduction. Journal of the American Chemical Society 144, 6613–6622.

Guo, B., Zeng, J., Brusseau, M.L., 2020. A mathematical model for the release, transport, and retention of per-and polyfluoroalkyl substances (PFAS) in the vadose zone. Water Resources Research 56, e2019WR026667.

Hazlett, R., 1995. Simulation of capillary-dominated displacements in microtomographic images of reservoir rocks. Transport in Porous Media 20, 21–35.

Hilpert, M., Miller, C.T., 2001. Pore-morphology-based simulation of drainage in totally wetting porous media. Advances in Water Resources 24, 243–255.

Jiang, H., Guo, B., Brusseau, M.L., 2020a. Pore-scale modeling of fluid-fluid interfacial area in variably saturated porous media containing microscale surface roughness. Water Resources Research 56, e2019WR025876.

Jiang, H., Guo, B., Brusseau, M.L., 2020b. Characterization of the microscale surface roughness effect on immiscible fluids and interfacial areas in porous media using the measurements of interfacial partitioning tracer tests. Advances in Water Resources 146, 103789.

Karagunduz, A., Pennell, K.D., Young, M.H., 2001. Influence of a nonionic surfactant on the water retention properties of unsaturated soils. Soil Science Society of America Journal 65, 1392–1399.

Lake, L.W., 1989. Enhanced Oil Recovery. Old Tappan, NJ; Prentice Hall Inc.

Lan, T., Hu, R., Su, X.N., Yang, Z., Chen, Y.F., 2025. Scaling of capillary pressure-saturation curve in porous media under various wetting conditions. Journal of Rock Mechanics and Geotechnical Engineering .

Leverett, M., 1941. Capillary behavior in porous solids. Transactions of the AIME 142, 152–169.

Li, Y., Sanfilippo, J.E., Kearns, D., Yang, J.Q., 2022. Corner flows induced by surfactant-producing bacteria Bacillus subtilis and Pseudomonas fluorescens. Microbiology Spectrum 10, e03233–22.

Liao, S., Arshadi, M., Woodcock, M.J., Saleeba, Z.S., Pinchbeck, D., Liu, C., Cápiro, N.L., Abriola, L.M., Pennell, K.D., 2022. Influence of residual nonaqueous-phase liquids (NAPLs) on the transport and retention of perfluoroalkyl substances. Environmental Science & Technology 56, 7976–7985.

Maroli, A.S., Zhang, Y., Lubiantoro, J., Venkatesan, A.K., 2024. Surfactant-enhanced coagulation and flocculation improves the removal of perfluoroalkyl substances from surface water. Environmental Science: Advances 3, 1714–1721.

Martys, N.S., Chen, H., 1996. Simulation of multicomponent fluids in complex three-dimensional geometries by the lattice boltzmann method. Physical review E 53, 743.

Millington, R., Quirk, J., 1961. Permeability of porous solids. Transactions of the Faraday Society 57, 1200–1207.

Or, D., Tuller, M., 1999. Liquid retention and interfacial area in variably saturated porous media: Upscaling from single-pore to sample-scale model. Water Resources Research 35, 3591–3605.

Øren, P.E., Bakke, S., 2003. Reconstruction of Berea sandstone and pore-scale modelling of wettability effects. Journal of Petroleum Science and Engineering 39, 177–199.

Patzek, T.W., 2001. Verification of a complete pore network simulator of drainage and imbibition. Spe Journal 6, 144–156.

Patzek, T.W., Kristensen, J.G., 2001. Shape factor correlations of hydraulic conductance in noncircular capillaries: II. Two-phase creeping flow. Journal of Colloid and Interface Science 236, 305–317.

Pope, G., Nelson, R., 1978. A chemical flooding compositional simulator. Society of Petroleum Engineers Journal 18, 339–354.

Qin, C.Z., van Brummelen, H., 2019. A dynamic pore-network model for spontaneous imbibition in porous media. Advances in Water Resources 133, 103420.

Raeini, A.Q., Blunt, M.J., Bijeljic, B., 2012. Modelling two-phase flow in porous media at the pore scale using the volume-of-fluid method. Journal of Computational Physics 231, 5653–5668.

Reeves, P.C., Celia, M.A., 1996. A functional relationship between capillary pressure, saturation, and interfacial area as revealed by a pore-scale network model. Water resources research 32, 2345–2358.

Rose, W., Bruce, W., 1949. Evaluation of capillary character in petroleum reservoir rock. Journal of Petroleum Technology 1, 127–142.

Silva, J.A.K., Šimůnek, J., McCray, J.E., 2020. A modified HYDRUS model for simulating PFAS transport in the vadose zone. Water 12, 2758.

Smith, J.E., Gillham, R.W., 1994. The effect of concentration-dependent surface tension on the flow of water and transport of dissolved organic compounds: A pressure head-based formulation and numerical model. Water Resources Research 30, 343–354.

Tokunaga, T.K., Wan, J., Jung, J.W., Kim, T.W., Kim, Y., Dong, W., 2013. Capillary pressure and saturation relations for supercritical CO_2 and brine in sand: High-pressure $P_c(S_w)$ controller/meter measurements and capillary scaling predictions. Water Resources Research 49, 4566–4579.

Tuller, M., Or, D., 2001. Hydraulic conductivity of variably saturated porous media: Film and corner flow in angular pore space. Water Resources Research 37, 1257–1276.

Tuller, M., Or, D., Dudley, L.M., 1999. Adsorption and capillary condensation in porous media: Liquid retention and interfacial configurations in angular pores. Water Resources Research 35, 1949–1964.

Valvatne, P.H., Piri, M., Lopez, X., Blunt, M.J., 2005. Predictive pore-scale modeling of single and multiphase flow. Transport in Porous Media 58, 23–41.

Wang, S., Tokunaga, T.K., Wan, J., Dong, W., Kim, Y., 2016. Capillary pressure-saturation relations in quartz and carbonate sands: Limitations for correlating capillary and wettability influences on air, oil, and supercritical CO_2 trapping. Water Resources Research 52, 6671–6690.

Wijnhorst, R., de Goede, T.C., Bonn, D., Shahidzadeh, N., 2020. Surfactant effects on the dynamics of capillary rise and finger formation in square capillaries. Langmuir 36, 13784–13792.

Yang, W., Brownlow, J.W., Walker, D.L., Lu, J., 2021. Effect of surfactant-assisted wettability alteration on immiscible displacement: a microfluidic study. Water Resources Research 57, e2020WR029522.

Young, T., 1805. An essay on the cohesion of fluids. Proceedings of the Royal Society of London Series I 1, 171–172.

Zeng, J., Guo, B., 2021. Multidimensional simulation of PFAS transport and leaching in the vadose zone: Impact of surfactant-induced flow and subsurface heterogeneities. Advances in Water Resources 155, 104015.

- Derive two-phase flow properties for surfactant/PFAS-laden fluids in angular porous media using a bundle-of-capillary-tubes model
- Formulate the two-phase flow properties as functions of interfacial tension, contact angle, and pore geometry and size distribution
- Derive explicit expressions and closed-form functions for the two-phase flow properties
- Couple explicit expressions and closed-form functions into a Darcy-scale two-phase flow and surfactant/PFAS transport model
- Example simulations highlight the critical role of pore angularity in PFAS transport and retention in unsaturated soils

Declaration of interests

☐ The authors declare that they have no known competing financial interests or personal relationships that could have appeared to influence the work reported in this paper.

☒ The authors declare the following financial interests/personal relationships which may be considered as potential competing interests:

Sidian Chen reports a relationship with Stanford University that includes: employment. If there are other authors, they declare that they have no known competing financial interests or personal relationships that could have appeared to influence the work reported in this paper.